

Abundance Discrepancy Factors in high density planetary nebulae

Francisco Ruiz-Escobedo^{1*}, Miriam Peña¹

¹*Instituto de Astronomía, Universidad Nacional Autónoma de México, Apdo. Postal 70264, Ciudad Universitaria, 04510 Ciudad de México*

Accepted XXX. Received YYY; in original form ZZZ

ABSTRACT

From high-resolution spectra, chemical abundances from collisionally excited lines (CELs) and optical recombination lines (ORLs) have been determined for planetary nebulae Cn 3-1, Vy 2-2, Hu 2-1, Vy 1-2 and IC 4997, which are young and dense objects. The main aim of this work is to derive their O^{+2}/H^+ Abundance Discrepancy Factors, ADFs, between CELs and ORLs. He, O, N, Ne, Ar, S, and Cl abundances were obtained and our values are in agreement with those previously reported. We found that Cn 3-1, Hu 2-1, and Vy 1-2 have O abundances typical of disc PNe, while Vy 2-2 and IC 4997 are low O abundance objects ($12 + \log(O/H) \sim 8.2$), which can be attributed to possible O depletion into dust grains. ADFs(O^{+2}) of $4.30^{+1.00}_{-1.16}$, 1.85 ± 1.05 , $5.34^{+1.27}_{-1.08}$ and $4.87^{+4.34}_{-2.71}$ were determined for Vy 2-2, Hu 2-1, Vy 1-2 and IC 4997, respectively. The kinematics of CELs and ORLs was analysed for each case to study the possibility that different coexisting plasmas in the nebula emit them. Expansion velocities of [O III] and O II are equal within uncertainties in three PNe, providing no evidence for these lines being emitted in different zones. Exception are Hu 2-1 and Vy 2-2, where ORLs might be emitted in different zones than CELs. For Vy 2-2 and IC 4997 we found that nebular and auroral lines of the same ion (S^+ , N^+ , Ar^{+2} , Ar^{+3} , O^{+2}) might present different expansion velocities. Auroral lines show lower V_{exp} which might indicate that they are emitted in a denser and inner zone than the nebular ones.

Key words: planetary nebulae: individual: Cn 3-1, Vy 2-2, Hu 2-1, Vy 1-2, IC 4997 – ISM:abundances – ISM:kinematics and dynamics

1 INTRODUCTION

Planetary nebulae (PNe) are constituted by shells of ionized gas expanding around an evolved hot central star which initially was a low-intermediate mass star ($1 - 8 M_{\odot}$) and it is on the way to become a white-dwarf. The shell was part of the stellar atmosphere and it was ejected in an advanced stage of evolution, during the AGB phase. Presently the central star has an effective temperature between 30,000 K to 150,000 K and typical properties of the ionized shell are: electron densities between 10^3 to 10^5 cm^{-3} , electron temperatures of about 10,000 K, and expansion velocities $V_{exp} \sim 20 - 30 \text{ km s}^{-1}$.

The ionized shell possesses a stratified structure, with the more ionized species nearer the central star. Usually the structure shows an expansion velocity gradient, with larger velocities towards the external zones where the less ionized species are found (Hubble law flow).

A large amount of heavy ions have been detected in the nebular spectra through Collisionally Excited Lines (CELs) of N^+ , O^+ , S^+ , S^{+2} , O^{+2} , Ne^{+2} , Ar^{+2} and even lines of O^{+3} , Ar^{+3} , Ar^{+4} and Ne^{+4} can be detected for the cases of very high stellar effective temperature. Optical Recombination Lines (ORLs) of H^+ , He^+ , He^{+2} are detected in the spectrum, and faint recombination lines of heavy elements (C, O, N, Ne, ...) have been detected also.

Physical conditions and ionic abundances relative to the H^+ abun-

dance can be derived from CELs as well as from ORLs. It has been found that the abundances of an ion determined from the two types of lines do not coincide, generally the abundances from recombination lines are larger than the ones derived from collisionally excited lines, giving origin to a discrepancy known as the Abundance Discrepancy Factor (ADF). Such a discrepancy has been object of numerous studies trying to understand its origin and to determine the true chemistry of the nebulae, which constitutes a fundamental parameter to understand the evolution of low-intermediate mass stars. Such ADFs are found in H II regions as well, with values usually between 1.5 and 3, see, e.g., Liu (2012); Esteban et al. (2014) and references therein, but in PNe it has a significant tail extending towards much larger values.

Several solutions have been proposed to explain the ADF problem (see Espíritu & Peimbert 2021, for a complete list). The two most important solutions have been extensively analysed. The first one is the presence of large temperature fluctuations in a chemically homogeneous plasma (Peimbert et al. 2014, and references therein); the fluctuations are larger than those predicted by photoionized models, and they have been used mainly to analyse ADFs in H II regions through the parameter t^2 that represents the size of the fluctuations (Esteban et al. 2014). The second solution corresponds to bi-abundance models where small H-deficient inclusions would be mixed with the H-rich hot plasma (Liu et al. 2000), these inclusions would be cold (T_e about 1,000 K) and heavy element recombination lines would originate predominantly in this plasma.

According to Peimbert et al. (2014), who analysed more than 20

* E-mail: fdruiz@astro.unam.mx

PNe, ADF values as large as 9 can be explained by the presence of thermal inhomogeneities in a chemically homogeneous plasma without requiring the presence of the small inclusions proposed by Liu et al. (2000). However in Peimbert et al. (2014) work the possibility of different plasmas of slightly different chemistry and physical conditions, coexisting in the nebulae, cannot be discarded. This possibility can be studied through kinematic analysis and it is the one that can be explored in this work where we analyse the chemistry and the kinematics in a sample of nebulae.

Since some years ago our group have started the analysis of several PNe to determine the physical conditions and chemistry in the ionized gas by using CELs and ORLs, by means of spectrophotometric data of high- and low-spectral resolution. In our previous work (Peña et al. 2017) and in works by other authors, evidence of different plasmas, with different chemistry and spatial location, existing in some nebulae, has been reported: one plasma is more widespread, it has low metallicity and high electron temperature, and it emits mainly the CELs, the other has larger heavy-element abundances and lower electron temperature, it is more concentrated towards the inner nebular zone and produces mainly the ORLs (see, e.g., García-Rojas et al. 2016; Richer et al. 2013).

In Peña et al. (2017), we analysed the kinematic of CELs and ORLs for a sample of 14 Galactic PNe with [WC] central star and ADFs ≤ 5 , finding that in several of them there is evidence of the existence of two different plasmas with different characteristics producing the CELs and ORLs, as mentioned above.

Our goal in this and upcoming articles is to enlarge that work and to determine the ADFs for O^{+2} of samples of PNe with different properties (central star types, low and high densities, different electron temperatures, different chemistry) to verify the validity of the hypothesis of two coexistent plasmas in PNe as a possible origin of the ADF, and to search for possible correlations of ADFs with some nebular characteristics. To do so, we analyse deep high-resolution spectra to determine physical conditions, abundances, and expansion velocities of CELs and ORLs, aiming to find if the emission of these lines arises from different regions within the nebulae.

In this work, we present the analysis carried out for five young, very high-density nebulae, three of which have been reported in the literature to show ADFs larger than 4. The objects under study are Cn 3-1 (PN G038.2+12.0), Vy 2-2 (PN G045.4-02.7), Hu 2-1 (PN G051.9-03.8), Vy 1-2 (PN G053.3+24.0), and IC 4997 (PN G058.3-10.9), whose main characteristics are presented in Table 1. Although some of these objects have been analysed previously by other authors, it is important to redetermine the physical conditions, the chemistry and the ADFs provided by CELs and ORLs in them in a homogeneous manner, by using the same procedures to analyse our data with up-to-date atomic parameters and to determine the uncertainties involved. In addition, we analyse the kinematic behaviour of CELs and ORLs that has not been done previously for these objects.

This paper is organised as follows. In §2 the PN characteristics, observations and data reduction procedures are given. In §3 the physical parameters derived from CELs and ORLs for each object, are presented. In §4 ionic abundances from CELs are calculated, while ionic abundances from ORLs are computed in §5. Total abundances are presented in §6. The nebular expansion velocities, derived for the different ions from their CELs and ORLs are discussed in §7. The results for individual nebulae can be found in §8. Our discussion and conclusions are presented in §9.

2 OBSERVATIONS AND DATA REDUCTION

To derive the chemical abundances from ORLs, high resolution spectra ($\delta\lambda$ better than $0.5 \text{ \AA}/\text{pix}$) are required because these lines appear generally blended with other ORLs or stellar lines. Therefore, for data acquisition we used the highest spectral resolution instrument available.

Some of the objects presented here have been observed by us since 2001, with the echelle REOSC spectrograph, attached to the 2.1-m telescope of the Observatorio Astronómico Nacional, at San Pedro Mártir, B.C., México, OAN-SPM. Most recent observations were carried out during September 2018, June and August 2019, with the same instrument, covering the wavelength range from about 3,600 Å to 7,000 Å. In all cases, the slit was located through the centre of the nebula crossing the central star position, and oriented E-W (P.A. 90°). The slit length was always 13.3 arcsec in the plane of the sky. The slit widths used were 100μ (1.3 arcsec) and 150μ (2 arcsec), which provided spectral resolutions $R = \lambda/\delta\lambda$ of 20,000 and 18,000, respectively, at 5,000 Å. Long and short exposure times were used in order to detect the weak lines (in particular the heavy-element recombination lines) with good signal to noise and to not saturate the intense lines (exposure times of 1,800 s, 900 s, 600 s or less were employed).

Wavelength calibration was performed with a Th-Ar lamp obtained after each scientific observation. Standard stars from the list by Hamuy et al. (1992) were observed each night for flux calibration. The slit width for standard stars was of 300μ (about 4 arcsec), in order to include all the stellar flux in the slit.

The log of observations is presented in Table 2. Observations obtained since 2001 are included.

2.1 Data reduction

Spectroscopic data were reduced following the IRAF¹ standard routines: set of BIAS obtained each night was combined in a MASTER-BIAS for BIAS subtraction. No flat field calibration was carried out. Spectra of the same object, obtained during a night, with the same exposure time, were combined in one, to improve the signal to noise. 1D spectra were extracted from the 2D echelle orders, they were wavelength calibrated with the Th-Ar lamp obtained after each observation and corrected by effects of atmospheric extinction, using the curve for OAN-SPM sky given by Schuster & Parrao (2001). Finally the flux calibration was carried out by using the standard stars spectra.

Spectra in the zone around $\lambda 4650$ are presented in Fig. 1 showing the quality of our data and the adequate spectral resolution to analyse the lines in this zone, which is very important to separate the O II and N II ORLs.

Fluxes were measured for all the available lines (which amount to more than 100 in each case), by using IRAF's *splot* task. Their "Full Width at Half Maximum", FWHM, were determined by applying a Gaussian fit in each case. If a line was double (two peaks) each component was measured and a Gaussian fit was applied to each one. Such lines are marked with an asterisk in the intensity tables. FWHMs were corrected by effects of instrumental width (derived from the line widths of comparison lamps) and thermal broadening (by adopting an electron temperature according to each case), by assuming they add in quadrature. Turbulent velocities were not considered (see §7).

¹ IRAF is distributed by the National Optical Astronomy Observatories, which is operated the Association of Universities for Research in Astronomy, Inc., under contract to the National Science Foundation.

Table 1. Characteristics of analysed PNe

Object	Name	$\log(F(H\beta))^a$ erg cm ⁻² s ⁻¹	Distance ^b (kpc)	Size arcsec	Morph. ^c	V_{rad} (km s ⁻¹)	ADF ^a (O ⁺²) W05	Star ^d	Comments References
PN G038.2+12.0	Cn 3-1	-10.94	4.68	4.8	Ec t * h	-11.8	—	O(H)7Ib	IRAS18152+1007 Gaia DR3
PN G045.4-02.7 ^e	Vy 2-2	-11.56	3.51	3.1x2.6	P	-71.2	11.8	B[e]	Lamers et al. (1998)
PN G051.4+09.6	Hu 2-1	-10.80	4.18	2.6	Bc bcr(o)	+17.0	4.0	WNb+?	Hipparcos distance
PN G053.3+24.0 ^f	Vy 1-2	-11.53	8.13	4.6	B fastOut	—	6.17	[WR]/wels	
PN G058.3-10.9	IC 4997	—	4.24	7.2	Bc t?	+07.2	—	wels	

^a Spectroscopy analysed by Wesson et al. (2005) (W05).

^b Distances from Frew et al. (2016), unless otherwise specified.

^c Morphology mostly from Sahai et al. (2011).

^d Star classification from Weidmann et al. (2020). For Vy 1-2 it is from Lamers et al. (1998).

^e Wide H α line due to Raman Effect, reported by Arrieta & Torres-Peimbert (2003).

^f A deep study of this nebula can be found in Akras et al. (2015)

Table 2. Log of observations

Object	Name	Obs. Date	Exp. Time (s)	Slit Size arcsec
PN G038.2+12.0	Cn 3-1	15/08/2019	3×1800, 900	2
PN G045.4-02.7	Vy 2-2	30/06/2019	3×1800	2
PN G051.4+09.6	Hu 2-1	13/08/2019	2×1800, 600	2
PN G053.3+24.0	Vy 1-2	21/09/2018	2×1800	1.3
PN G058.3-10.9	IC 4997	25/08/2001	900, 60	4

Table 3. Logarithmic reddening correction and assumed temperatures and densities for the theoretical Balmer ratios used in the calculation

Object	$c(H\beta)$	T_e (10 ⁴ K)	$\log(n_e)$ (cm ⁻³)	H/H β (avg)
Cn 3-1	0.65±0.07	0.75	4	H α , H γ , H δ , H ϵ
Vy 2-2	0.66±0.01	1.00	4	H α
Hu 2-1	0.45±0.05	1.00	4	H γ , H δ
Vy 1-2	0.31±0.06	1.00	4	H α , H γ , H δ
IC 4997	0.32±0.01	1.50	6	H γ

Line flux errors were calculated by using the Tresse et al. (1999) expression shown here:

$$\sigma_F = \sigma_c D \sqrt{2N_{\text{pix}} + \frac{EW}{D}} \quad (1)$$

where D is the spectral dispersion in $\text{\AA}/\text{pix}$, σ_c is the mean standard deviation per pixel of the continuum measured on each side of the line, and N_{pix} is the number of pixels covered by the line. For the upcoming calculations, we adopted $2\sigma_F$ values as more adequate to represent the true line errors.

For each observed object, the logarithmic reddening correction, $c(H\beta)$, was derived by using Cardelli et al. (1989) reddening law, assuming a ratio of total to selective extinction $R_V = 3.1$ and by using the different theoretical ratios $H\alpha/H\beta$, $H\gamma/H\beta$, $H\delta/H\beta$ and $H\epsilon/H\beta$ given by Storey & Hummer (1995) for the temperatures and densities presented for each object in Table 3. H α line was saturated in the spectra of Hu 2-1 and IC 4997, even in their low exposure-times spectra, therefore the H α /H β ratio was not used.

The observed and de-reddened fluxes and the corrected line widths for each object are presented in individual tables. Such tables can be

found in the on-line version only. An example of such tables is presented in Table 4 for Cn 3-1, where the emitting ion, the wavelength at rest, the observed central wavelength, the observed and de-reddened fluxes, relative to H β , and their uncertainties obtained by propagating the errors associated to the line fluxes through the normalization to H β and the de-reddening correction, are presented together with the line widths (FWHM) and the expansion velocities derived from the line widths. The individual tables of all PNe are available as online supplementary data.

3 PHYSICAL PARAMETERS OF NEBULAE

From the nebular lines, in particular from those collisionally excited lines, physical conditions, such as electron densities and temperatures, can be derived from some diagnostic line ratios. Densities can be determined from the [S II] $\lambda\lambda 6731/6716$, [O II] $\lambda\lambda 3729/3726$, [Cl III] $\lambda\lambda 5538/5518$, [Fe III] $\lambda\lambda 4701/4659$, and [Ar IV] $\lambda\lambda 4711/4740$ intensity ratios. Electron temperatures can be obtained from the [N II] $\lambda\lambda(6548+6584)/5755$, [O III] $\lambda\lambda(5007+4959)/4363$, [Ar IV] $\lambda\lambda(7170+7263)/(4711+4740)$, [S II] $\lambda\lambda(6716+6731)/(4068+4076)$ and [O II] $\lambda\lambda 7325/3727$ intensity ratios.

From the available diagnostic line ratios, all densities and temperatures were calculated with the code PYNEB (Luridiana et al. 2015), using the atomic data presented in the Appendix A, Table A1. PYNEB routine *getCrossTemden* was used to determine simultaneously the temperature and density from the [N II], [O III], [S II] and other diagnostic lines, by building diagnostic diagrams. The uncertainties in the physical conditions and abundances were estimated using Monte Carlo simulations, with 400 random points following a normal distribution around the observed intensity of the lines.

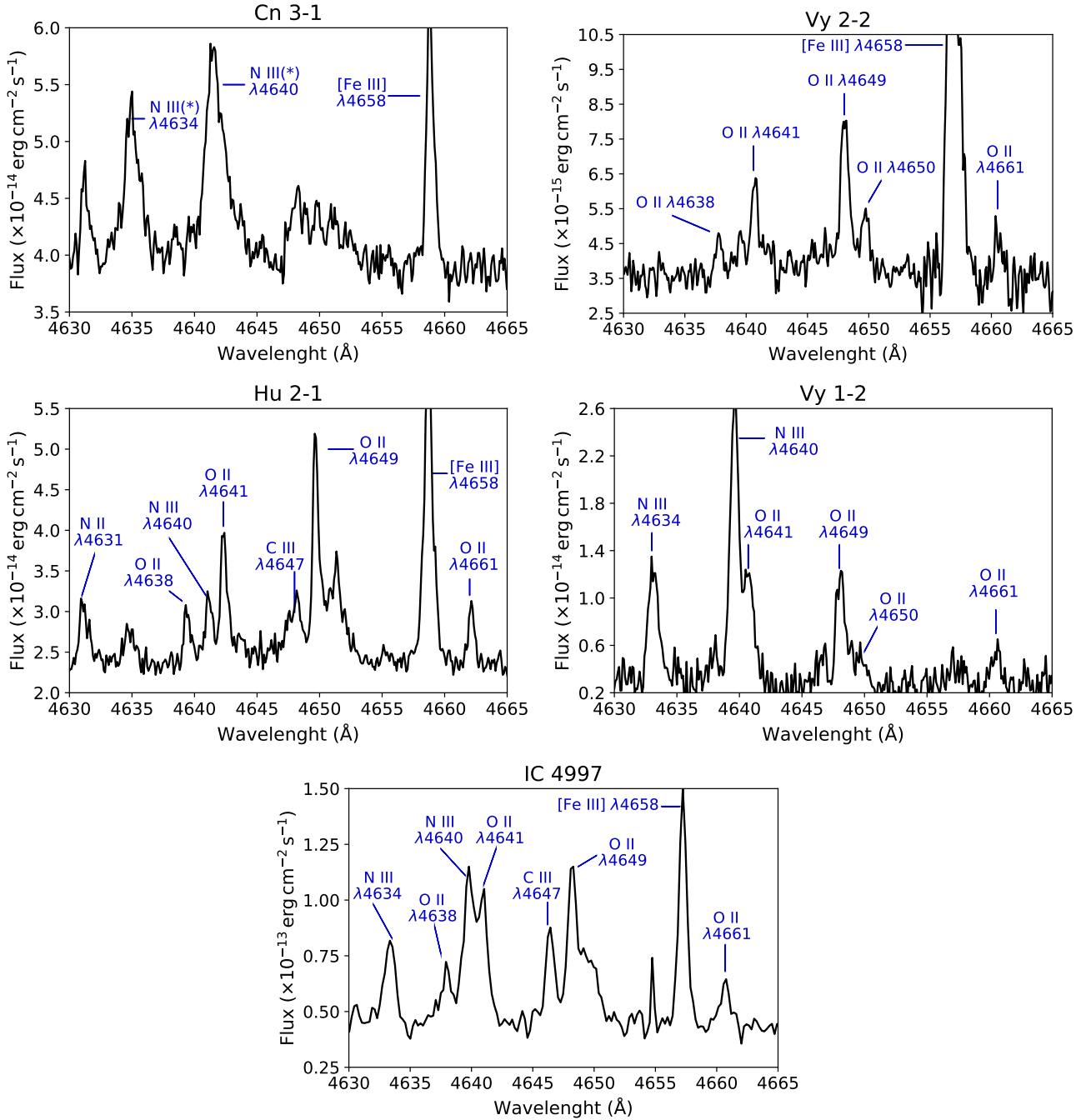


Figure 1. Section of the calibrated spectra of the sample, around 4650 Å. Important recombination lines of heavy elements are highlighted. An asterisk in the line identification indicates that the line is emitted by the central star and not by the nebula.

3.1 Diagnostics diagrams

In Fig. 2 diagnostic diagrams for the analysed objects are presented. These diagrams show the behaviour of diagnostic line ratios with the electron density and temperature. Each line ratio is represented by a broken or dotted line inside a colour band which shows the 1σ rms error. Usually the electron densities and temperatures are obtained from the zone where density- and temperature-diagnostics intersect. The derived values for our objects are listed in Table 5. These temperatures and densities will be used to determine ionic abundances.

In order to derive correct temperatures, intensities of the auroral lines [N II] $\lambda 5755$ and [O III] $\lambda 4363$ were corrected by effects of recombination using Liu et al. (2000) relations:

$$\frac{I_R(\lambda 5755)}{I(H\beta)} = 3.19 t^{0.30} \times \frac{N^{+2}}{H^+}, \quad (2)$$

where $t = T_e([N II])/10^4 K$, and $\frac{N^{+2}}{H^+}$ is the abundance determined from recombination lines.

Table 4. Example: Cn 3-1: observed (F_λ) and de-reddened (I_λ) fluxes normalized to $H\beta = 100$, their absolute errors, line widths FWHM and expansion velocities. Tables for all objects are available as on-line material

Ion	λ_0 (Å)	λ_{obs} (Å)	$F_\lambda/F(H\beta)$	$\delta(F_\lambda)$	$I_\lambda/I(H\beta)$	$\delta(I_\lambda)$	$V_{\text{rad hel}}$ (km s ⁻¹)	FWHM (Å)	v_{exp} (km s ⁻¹)
He I	3634.25	3634.84	0.16	0.02	0.26	0.03	30.14	0.32	13.39
H29	3663.40	3663.98	0.15	0.02	0.24	0.04	29.18	0.54	22.18
H28	3664.68	3665.21	0.19	0.02	0.31	0.03	24.99	0.39	15.81
H27	3666.10	3666.65	0.23	0.02	0.38	0.03	26.78	0.31	12.50
H26	3667.68	3668.21	0.22	0.02	0.36	0.04	24.96	0.40	16.37
H25	3669.46	3669.97	0.28	0.02	0.46	0.04	23.71	0.48	19.77
H24	3671.48	3672.04	0.29	0.02	0.48	0.03	27.36	0.59	24.13
H23	3673.76	3674.28	0.43	0.01	0.69	0.04	24.31	0.49	19.94
H22	3676.36	3676.93	0.40	0.02	0.65	0.04	27.88	0.43	17.54
H21	3679.36	3679.88	0.40	0.02	0.66	0.04	24.17	0.47	19.33
H20	3682.81	3683.38	0.62	0.02	1.00	0.05	28.04	0.52	21.18
H19	3686.83	3687.42	0.58	0.03	0.94	0.06	29.53	0.50	20.38
H18	3691.56	3692.15	0.74	0.03	1.19	0.07	29.72	0.55	22.32
H17	3697.15	3697.76	0.85	0.02	1.38	0.07	31.27	0.54	21.90
H16	3703.86	3704.42	0.81	0.02	1.32	0.07	27.37	0.46	18.46
He I	3705.04	3705.57	0.16	0.02	0.25	0.04	24.28	0.47	18.88
H15	3711.97	3712.53	1.18	0.02	1.91	0.09	27.19	0.46	18.57
H14	3721.83	3722.45	1.66	0.03	2.69	0.13	31.83	0.50	20.23
[O III]	3726.03	3726.58	66.26	0.12	107.29	4.78	26.38	0.41	16.62
[O II]	3728.82	3729.33	30.44	0.08	49.28	2.20	23.04	0.39	15.81
...									

For [O III] λ 4363, the expression used is:

$$\frac{I_{\text{R}}(\lambda 4363)}{I(H\beta)} = 12.4 t^{0.59} \times \frac{O^{+3}}{H^+}, \quad (3)$$

where $t = T_e([\text{O III}])/10^4 \text{ K}$ and $\frac{O^{+3}}{H^+}$ is the abundance determined from recombination lines. This correction was only applied to Vy 1-2 which is the only highly ionized object of the sample. As the observed lines of O III are emitted by Bowen resonance and not by pure recombination (Grandi 1976; García-Rojas et al. 2013), we could estimate $\frac{O^{+3}}{H^+}$ using the next relation, given by Kingsburgh & Barlow (1994):

$$\frac{O^{+3}}{H^+} = \left[\left(\frac{\text{He}}{\text{He}^+} \right) - 1 \right] \times \left(\frac{O^+}{H^+} + \frac{O^{+2}}{H^+} \right) \quad (4)$$

In this case we used the O^+ and O^{+2} abundances determined from CELs because we were not able to determine the abundance of O^+ from recombination lines.

For Vy 1-2, we determined that the recombination contribution to auroral line [O III] λ 4363 intensity is of $\sim 1\%$. We also found the same percentage using the recent relation proposed by Gómez-Llanos et al. (2020) for this correction. The T_e determined using the uncorrected auroral line intensity is about $\sim 200 \text{ K}$ higher than that determined using the corrected line intensity, which lies within the error bars. Therefore the correction does not produce a significant effect in abundances determinations. In addition, García-Rojas et al. (2012) were able to determine O^{+3} abundance directly from ORLs for the highly ionized PNe of their sample, they found that the recombination contribution is about $\sim 3\%$ and the correction was negligible in the temperature determinations.

3.2 Physical parameters from ORLs

In this section the techniques used to derive electron densities and temperatures from recombination lines are described. Temperature

can be derived from the He I lines, from the O II lines, and from the Balmer Jump as explained in the following.

3.2.1 Temperatures from the Balmer Jump

Temperature from the Balmer jump, $T_e(\text{BJ})$, was only determined for Cn 3-1, Hu 2-1 and IC 4997. We followed the procedure given by Liu et al. (2001) for $T_e(\text{BJ})$ determination:

$$T_e(\text{BJ}) = 368 \times (1 + 0.259 y^+ + 3.409 y^{++}) \left(\frac{\text{BJ}}{I(\text{H11})} \right)^{-3/2} \text{ K}, \quad (5)$$

where y^+ and y^{++} are the ionic abundances He^+/H^+ and He^{+2}/H^+ , respectively, $\text{BJ} = I_c(3643) - I_c(3681)$ is the subtraction of intensities of the continuum at those wavelengths, and $I(\text{H11})$ is the intensity of H I λ 3770.

3.2.2 Temperatures from He I lines

Helium electronic temperatures, $T_e(\text{He I})$, can be derived using Zhang et al. (2005) methodology and the theoretical emissivities for He I lines by Benjamin et al. (1999). We were able to determine temperatures from the line ratios $\lambda\lambda 7281/6678$, $\lambda\lambda 7281/5875$, $\lambda\lambda 6678/5875$, $\lambda\lambda 6678/4471$ and $\lambda\lambda 5875/4471$, by assuming a density of 10^4 cm^{-3} , which agrees with the values derived from recombination lines (see Table 7).

Zhang et al. (2005) and Otsuka et al. (2010) suggested that the most accurate line ratio to determine $T_e(\text{He I})$ is $\lambda\lambda 7281/6678$, because these lines are among the most intense He I lines in the optical range, their ratio is more sensitive to temperature but less sensitive to density than other He I lines ratios, their recombination coefficients are more reliable than those for He I λ 4471 and λ 5876, and their ratio is less affected by the effect of the interstellar extinction because of their close wavelengths.

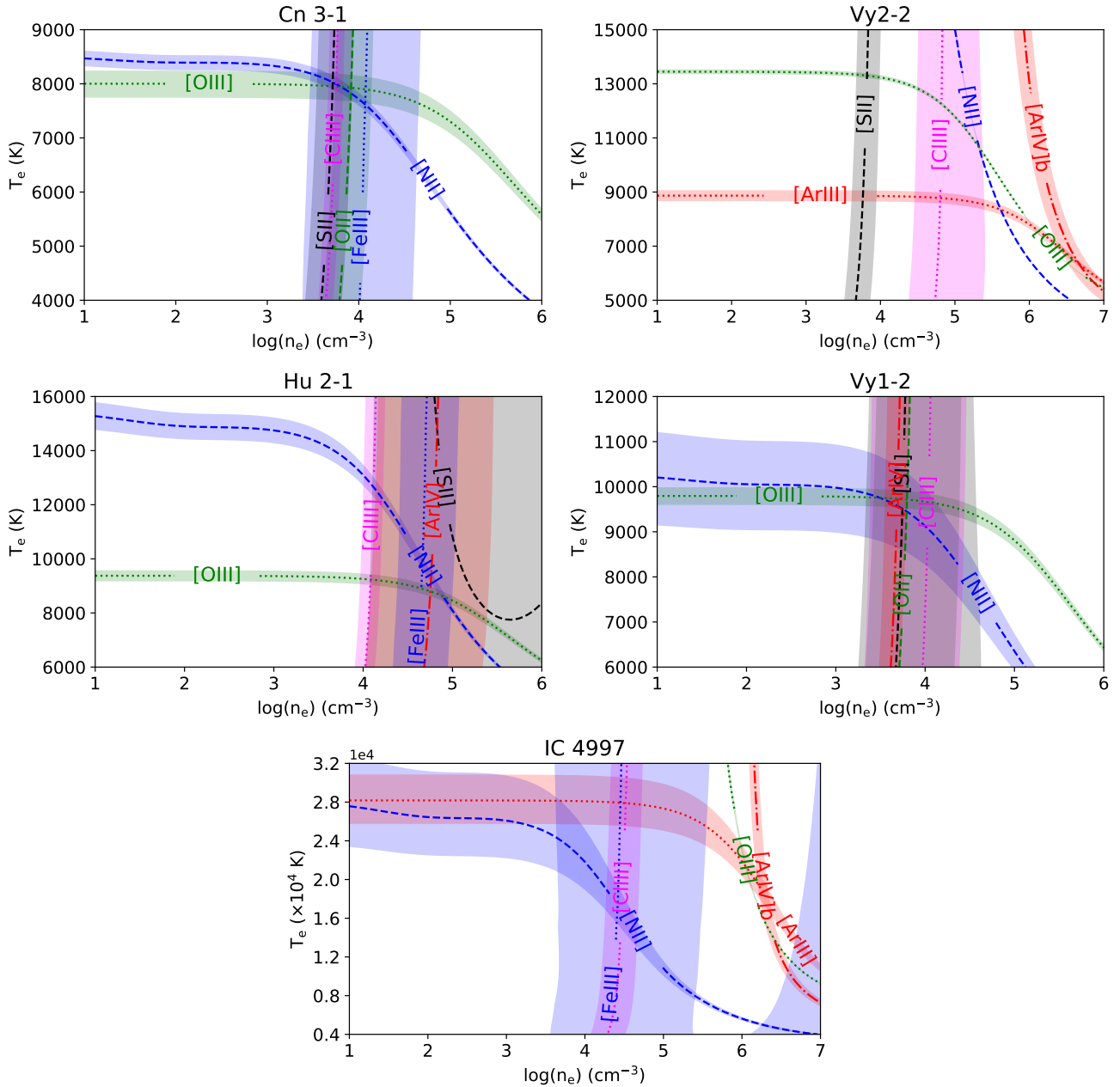


Figure 2. Diagnostic diagrams for density and temperature, derived with `PYNEB`, for the different objects. Sensitive CELs line ratios are indicated. Coloured shadowed bands represent the 1 sigma rms error of each diagnostic. [Ar IV]b represents the line ratio $\lambda\lambda 7170/4740$.

Unfortunately, we could only measure the intensity of He I $\lambda 7281$ in two objects of our sample. In those objects where this line could not be measured we adopted as $T_e(\text{He I})$ the temperature derived from the line ratio $\lambda\lambda 6678/5875$. We made this assumption because the determined $T_e(\text{He I})$ from $\lambda\lambda 7281/6678$ and $\lambda\lambda 6678/5875$ are very close, within the uncertainties, for Vy 2-2 and IC 4997; this result was also found by *Otsuka et al. (2010)* for the halo PN BoBn 1.

3.2.3 Temperatures and densities from O II

It is known that the emissivities of recombination lines have a weak dependence on electronic temperature ($I_{\text{ORLS}} \sim T_e^{-1}$), nonetheless, some lines of O II emitted from states with different orbital an-

gular momenta show some dependence on electronic temperature, thus they can be used to estimate the temperature in the zone where O II lines are being emitted. This methodology, first used by *Wesson et al. (2003)* and then supported by some other authors (*Tsamis et al. 2004; Wesson et al. 2005; Fang & Liu 2013; McNabb et al. 2013*), uses the intensity ratio $\lambda\lambda 4649/4089$, lines emitted in different transitions, as temperature indicator. The results presented by these works show that $T_e(\text{O II})$ are very low compared to T_e from CELs, and follow a tendency of temperature values $T_e([\text{O III}]) \geq T_e(\text{BJ}) \geq T_e(\text{He I}) \geq T_e(\text{O II})$. The main disadvantage of this method is that O II $\lambda 4089$ line is very faint and is difficult to measure. In this work, this O II line could only be detected in the spectra of Hu 2-1 and IC 4997, therefore only for these two objects $T_e(\text{O II})$ could be determined using this method.

Table 5. Electron densities and temperatures^(a) from collisionally excited lines

	Line ratio	Cn 3-1	Vy 2-2	Hu 2-1	Vy 1-2	IC 4997
n_e [S II]	6731/6716	5,100 ^{+3,000} _{-1,500}	6,200 ^{+3,000} _{-1,800}	—	4,600 ^{+8,200} _{-2,300}	—
n_e [O II]	3729/3726	7,900 ^{+5,000} _{-2,400}	—	—	5,100 ^{+8,700} _{-2,500}	—
n_e [Cl III]	5538/5518	5,600 ^{+1,100} ₋₈₀₀	58,200 ^{+76,600} _{-23,200}	13,200 ^{+4,200} _{-2,700}	9,300 ^{+15,800} _{-5,300}	31,700 ^{+21,100} _{-11,200}
n_e [Fe III]	4701/4659	10,500 ^{+16,200} _{-6,700}	—	32,300 ^{+53,900} _{-11,200}	—	23,200 ^{+340,500} _{-18,200}
n_e [Ar IV]	4740/4711	—	—	48,700 ^{+88,000} _{-27,100}	4,800 ^{+1,400} _{-1,200}	—
<i>Adopted</i>		6,600 ^{+2,100} _{-1,400}	1) 6,200 ^{+3,000} _{-1,800} 2) 58,200 ^{+76,600} _{-23,200}	1) 13,200 ^{+4,200} _{-2,700} 2) 47,100 ^{+79,000} _{-21,000}	5,400 ^{+5,200} _{-1,600}	1) 31,700 ^{+21,100} _{-11,000} 2) 1.81 ^{+0.90} _{-0.48} × 10 ⁶ ^(b)
T_e [N II]	(6584+6548)/5755	7,800±200	—	10,200 ^{+1,100} _{-1,800}	9,300 ^{+1,100} _{-1,500}	16,200 ^{+3,100} _{-2,800}
T_e [O III]	(5007+4959)/4363	8,100±200	12,800±600	9,000±300 ^(c)	9,700±200	—
T_e [Ar III]	7136/5192	—	8,800±200	—	—	—
<i>Adopted</i>		7,900±200	1) 8,800±200 2) 12,800±600	9,300 ^{+1,100} _{-1,500}	9,500±500	16,200 ^{+3,100} _{-2,800}

(a): electron densities in particles cm⁻³, temperatures in K

(b): n_e from [O III] $\lambda\lambda 4959/4363$

(c): $\lambda 5007$ line is saturated, T_e was determined from $\lambda\lambda 4959/4363$

Table 6. Adopted zones and their physical conditions for CELs ionic abundance determinations

PN	Zone	Ions	n_e (cm ⁻³)	T_e (K)
Cn 3-1	1	All observed	6,600 ^{+2,140} _{-1,400}	7,900±200
Vy 2-2	1	N ⁺ , O ⁺ , S ⁺ , Fe ⁺	6,200 ^{+3,000} _{-1,800}	8,800±200
	2	Fe ⁺² , S ⁺² , Cl ⁺² , Ar ⁺²	58,200 ^{+76,600} _{-23,200}	8,800±200
	3	O ⁺² , Ne ⁺² , Ar ⁺³	58,200 ^{+76,600} _{-23,200}	12,800±600
Hu 2-1	1	N ⁺ , O ⁺ , S ⁺ , Fe ⁺ , S ⁺² , Ar ⁺² , O ⁺² , Cl ⁺²	13,200 ^{+4,200} _{-2,700}	9,300 ^{+1,100} _{-1,500}
	2	Fe ⁺² , Ne ⁺² , Ar ⁺³	47,100 ^{+79,000} _{-21,000}	9,300 ^{+1,100} _{-1,500}
Vy 1-2	1	All observed	5,400 ^{+5,400} _{-1,600}	9,500±500
IC 4997	1	N ⁺ , O ⁺ , S ⁺ , Fe ⁺² , Cl ⁺² , S ⁺²	31,700 ^{+21,000} _{-11,000}	16,200 ^{+3,100} _{-2,800}
	2	O ⁺² , Ar ⁺² , Ne ⁺² , Ar ⁺³	1.81 ^{+0.90} _{-0.48} × 10 ⁶	16,200 ^{+3,100} _{-2,800}

Another way to estimate T_e (O II) is by using the relationship proposed by Peimbert et al. (2014). This method is based on the rate of line intensities from both CELs and ORLs of O⁺² and relates their intensities with the electron temperature.

$$\frac{I(V1)}{I(F1)} = 1.772 \cdot 10^{-5} \left(\frac{T_e}{10,000 \text{ K}} \right)^{-0.40} \exp \left(\frac{29,170 \text{ K}}{T_e} \right), \quad (6)$$

where I(V1) is the intensity of all the lines of the V1 multiplet of O II and I(F1) is the sum of the intensities of [O III] $\lambda 5007$ and $\lambda 4959$. V1 multiplet is constituted by the lines $\lambda\lambda 4638, 4642, 4649, 4651, 4661, 4673, 4676, 4696$; and in LTE, the intensity of $\lambda 4649$ represents the 39.7% of the total multiplet intensity (Peimbert et al. 2014).

On the other side, the relative population of the ground-term fine-structure levels of some recombining ions, such as O II and N II, vary with the electron density. From the intensity ratio of two ORLs emitted in the same multiplet but from different parent levels, one can determine the electronic density (Fang & Liu 2013). These authors show that line ratios O II $\lambda\lambda 4649/4661$ and N II $\lambda\lambda 5679/5666$ are useful for the electronic density calculation. In our work we were

able to determine the densities from O II $\lambda\lambda 4649/4661$ for Vy 2-2, Vy 1-2, Hu 2-1 and IC 4997.

All the results obtained from the methods described above are listed in Table 7.

4 IONIC ABUNDANCES FROM CELS

Ionic abundances for O⁺, O⁺², N⁺, Ne⁺², Ne⁺³, S⁺, S⁺², Cl⁺², Ar⁺², Ar⁺³, Ar⁺⁴, Fe⁺, Fe⁺², and others, were determined from CELs using the task *get.IonAbundance* from PYNEB. For this we used the de-reddened intensities of the lines listed in Table 8 as measured for each nebula, and the adopted physical conditions for each nebular zone as presented in Table 6. The results for all the objects are given in Table 10. In the following the adopted zones for each case are presented.

Table 7. Electron densities (in cm^{-3}) and temperatures (in K) derived from recombination lines

	Cn 3-1	Vy 2-2	Hu 2-1	Vy 1-2	IC 4997
$n_e(\text{O II})$ 4649/4661	—	19,900±4,300	31,600±18,000	7,900±4,300	5,000±2,500
$T_e(\text{BJ})$	7,600±200	—	7,700±400	—	11,300±700
$T_e(\text{He I})$ 7281/6678	—	8,300±300	—	—	8,900 ^{+1,100} ₋₈₀₀
$T_e(\text{He I})$ 7281/5875	—	8,600±400	—	—	8,000 ^{+1,400} ₋₉₀₀
$T_e(\text{He I})$ 6678/5875	—	7,600±500	6,900±1,500	8,800±3,200	10,500±1,100
$T_e(\text{He I})$ 6678/4471	—	5,900±400	5,800±300	7,300±3,000	3,900 ⁺⁶⁰⁰ ₋₃₀₀
$T_e(\text{He I})$ 5875/4471	3,100±400	4,300±700	2,500±300	3,900±1,900	4,200 ^{+1,300} ₋₆₀₀
$T_e(\text{He I})$ <i>Adopted</i> ¹	7,600±200	8,300±300	6,600±1,300	8,800±3,200	8,900 ^{+1,100} ₋₈₀₀
$T_e(\text{O II})$ (P14)	—	8,000±300	7,900±100	6,400±100	7,100±100
$T_e(\text{O II})$ 4649/4089	—	—	2,900:	—	2,700:
$T_e(\text{O II})$ <i>Adopted</i> ²	7,600±200	8,000±300	7,900±100	6,400±100	7,100±100

1: Adopted for the determination of He^+ abundances.

2: Adopted for the determination of O^{+2} , N^{+2} and C^+ abundances.

: represents a very uncertain result.

4.1 Cn 3-1

For this object we assumed a single zone of temperature and density for all the ionic species. The adopted temperature is the mean value of the temperatures derived from $[\text{N II}]$ and $[\text{O III}]$ line ratios, which are equal within uncertainties. The density was determined as the mean value of the computed densities from $[\text{S II}]$, $[\text{O II}]$ and $[\text{Cl III}]$ line ratios. The density from $[\text{Fe III}]$ which is higher, was not considered as the $[\text{Fe III}]$ lines are very faint and the derived density has large uncertainty (see the 1σ error band in Fig. 2). Thus, Cn 3-1 is assumed to be a nebula with a single zone of temperature and density with values $T_e \sim 7,900$ K and $n_e \sim 6,600$ cm^{-3} .

4.2 Vy 2-2

At least two density zones were found in this object: a low density zone given by the $[\text{S II}]$ diagnostic with a value of $n_e \sim 6,200$ cm^{-3} ; and a high density zone given by the $[\text{Cl III}]$ diagnostic with a value $n_e \sim 58,200$ cm^{-3} , almost ten times larger than that of the low density zone. Most probably there is a gradient of density increasing inwards in this object. For the single ionized species the density from $[\text{S II}]$ ratio was used, while for the twice or more ionized species the density from $[\text{Cl III}]$ ratio was used. Regarding the electron temperature, the $[\text{N II}]$ $\lambda\lambda(6548+6584)/5755$ line ratio cannot be used as temperature diagnostic due to the nebular lines are highly affected by the inner high density, therefore these lines are undergoing collisional de-excitation. Thus the $[\text{N II}]$ ratio is more indicative of density, showing a value of about 10^5 cm^{-3} (see Fig. 2). The same occurs with the temperature sensitive $[\text{Ar IV}]$ $\lambda\lambda 7170/4740$, which in this case is indicating a density of about 10^6 cm^{-3} for the highest ionized zone. Then the only available temperature diagnostics are the $[\text{O III}]$ and $[\text{Ar III}]$ line ratios providing temperatures of about 12,800 K and 8,800 K, respectively. We decided to adopt the temperature given by $[\text{Ar III}]$ for the low ionized species, and $T_e([\text{O III}])$ for the high ionized species, as indicated in Table 6.

4.3 Hu 2-1

Densities were derived from $[\text{Cl III}]$, $[\text{Fe III}]$ and $[\text{Ar IV}]$ diagnostics, with values of $13,200$ cm^{-3} , $32,300$ cm^{-3} and $48,700$ cm^{-3} , respectively. The $[\text{O II}]$ and $[\text{S II}]$ density diagnostic ratios could not be

calculated with `PYNEB` routines due to apparent problems with atomic parameters. As it is shown in Fig. 2 the $[\text{S II}]$ line ratio is useless for density determination. On the other hand, the $[\text{O II}]$ density, previously determined by Wesson et al. (2005) and Delgado-Inglada et al. (2015), with a value of $\sim 7,000$ cm^{-3} can be adopted. Thus Hu 2-1 is a nebula with increasing density inwards.

For the single and double ionized species we adopted the density given by the $[\text{Cl III}]$ and for the triple ionized species we adopted the mean value of $[\text{Fe III}]$ and $[\text{Ar IV}]$ densities, $47,100$ cm^{-3} . An electron temperature of 10,200 K was determined from $[\text{N II}]$ lines, and a value of 9,000 K from the $[\text{O III}]$ lines in the zone were both diagnostics cross with $[\text{Ar IV}]$ density diagnostic. Therefore we assumed a single temperature for the whole nebula of 9,300 K, given by the mean value of $[\text{N II}]$ and $[\text{O III}]$ temperatures.

4.4 Vy 1-2

In this case we adopted a single zone of density and temperature for all species. Density is given by the mean value of $[\text{S II}]$, $[\text{O II}]$, and $[\text{Ar IV}]$ diagnostics and leads to a value of $5,400$ cm^{-3} . The slightly larger density provided by the $[\text{Cl III}]$ lines was not considered, due to the large uncertainty this value presents (see the wide 1σ pink error band in Fig. 2). The temperature was determined as the mean value of $[\text{N II}]$ and $[\text{O III}]$ diagnostics which are very similar, leading a value of 9,500 K.

4.5 IC 4997

This is a very complex object. Hyung et al. (1994), by analysing optical and ultraviolet spectra, concluded that this PN contains at least two important density zones: an outer zone with $n_e \sim 10^4$ cm^{-3} and an inner one with $n_e \sim 10^6 - 10^7$ cm^{-3} . One important detail about IC 4997 is the low $[\text{O III}]$ $\lambda\lambda 4959/4363$ line ratio which shows a present value ~ 2.05 . This ratio has been decreasing with time (Arkhipova et al. 2017). This low value is caused by the high intensity of the auroral line $\lambda 4363$, augmented due to the large nebular density (Menzel et al. 1941), and the low intensity of the nebular lines which, as a consequence of the density larger than the critical value for these lines, are undergoing collisional de-excitation. Therefore, it is more appropriate to use the ratio of the nebular to auroral line as a

Table 8. Collisionally excitation lines used for ionic abundances determinations

X ⁺ⁱ	Line
N ⁺	[N II] $\lambda\lambda 6548, 6584$
O ⁺	[O II] $\lambda\lambda 3727, 3729$
O ⁺²	[O III] $\lambda\lambda 4959, 5007$
Ne ⁺²	[Ne III] $\lambda\lambda 3868, 3967$
Ne ⁺³	[Ne IV] $\lambda 4724$
S ⁺	[S II] $\lambda\lambda 6716, 6731$
S ⁺²	[S III] $\lambda 6712$
Cl ⁺²	[Cl III] $\lambda\lambda 5517, 5537$
Ar ⁺²	[Ar III] $\lambda\lambda 5192, 7136$
Ar ⁺³	[Ar IV] $\lambda\lambda 4711, 4740$
Ar ⁺⁴	[Ar V] $\lambda 7005$
Fe ⁺	[Fe II] $\lambda 7155$
Fe ⁺²	[Fe III] $\lambda\lambda 4659, 4701, 4734, 4755$
K ⁺³	[K IV] $\lambda 6102$

density diagnostic instead of a temperature one (e.g., [Kingsburgh & Barlow 1994](#); [Wesson et al. 2005](#)). Thus this ratio leads to a value of $n_e \sim 1.81 \times 10^6 \text{ cm}^{-3}$.

The diagnostic diagram for this object (Fig. 2) is very complex. Our interpretation is that there are, at least, two very different density-zones: one given by [Cl III] and [Fe III] line ratios, of about $31,700 \text{ cm}^{-3}$, and a second one given by [O III] and [Ar III] line ratios which is larger than about $1.81 \times 10^6 \text{ cm}^{-3}$. The [Ar IV] temperature diagnostic line ratio, density-sensitive for this case, also indicates such a high density. It was also possible to estimate the density given by [S II] lines but this diagnostic is in the limit of its validity range and the interpretation is inconclusive, therefore it is not presented in the diagram.

The [N II] diagnostic ratio is the only one useful to estimate the electron temperature. The intersection between this ratio and the [Cl III] density diagnostics results in a $T_e = 16,200 \text{ K}$ and $n_e = 31,700 \text{ cm}^{-3}$. We adopted only the density value of [Cl III] because of the high dispersion of [Fe III] density. When we assumed this T_e for the inner zones, we found $n_e([O III]) = 1.81 \times 10^6 \text{ cm}^{-3}$. To determine ionic abundances, we decided to adopt a single temperature zone and two different density zones, given by [Cl III] and [O III] ratios; they are shown in Table 6.

5 IONIC ABUNDANCES FROM ORLS: THE ADFS

Ionic abundances from ORLS were computed using `PYNEB.get.IonAbundance` with the previously determined temperatures and densities ($T_e(\text{He I})$, $T_e(\text{O II})$ or $T_e(\text{BJ})$) presented in Table 7. We adopted the density derived from O II $\lambda\lambda 4661/4649$ to determine ionic abundances from recombination lines, except for Cn 3-1 where it was not possible to estimate it and thus the density determined from forbidden lines was adopted. Adopted temperatures were different in each case: for He I we adopted the derived $T_e(\text{He I})$, for He II in Vy 1-2, the temperature determined from CELs, and for heavy elements, $T_e(\text{O II})$ derived from [Peimbert et al. \(2014\)](#) expression. We decided not to use $T_e(\text{O II})$ determined in Hu 2-1 and in IC 4997 from line ratio $\lambda\lambda 4649/4089$ due to their very large uncertainties. For Cn 3-1 we used $T_e(\text{BJ})$ to determine the abundances of all recombination lines.

For each ion, different line intensities were used: $\lambda 5875$ for He I, $\lambda 4686$ for He II, $\lambda 4267$ for C II, the intensities of V1 multiplet for O II and the intensities of multiplet V3 for N II.

The results for O⁺², C⁺², and N⁺² are presented in Table 9. The O⁺² values, compared to the ionic abundances from CELs, for the same ion, allow us to derive the ADFs that are presented in Table 11.

6 ABUNDANCE RESULTS

Total abundances from CELs were calculated from the measured ionic abundances and using Ionization Correction Factors, ICFs, to correct for the unseen ions. The ICFs employed and their expressions are presented in Appendix B. Values for ICFs are listed in Table 10 together with the total abundances derived for each object.

In §8 we discuss the derived abundances, together with the kinematics, for each case.

7 THE KINEMATICS

The expansion velocity of the different ions as a function of their ionization potential has been analysed. Due to the ionization structure of the nebulae, the ionization potential approximately represents the distance of the ion to the central star. Fig. 3 shows these behaviours, including the expansion velocities given by CELs (in blue) and by ORLS (in red). Each dot represents the average value of the expansion velocities of the observed lines of each ion, while the error bars represent their mean standard deviation. When only a single line was available, we adopted 2 km s^{-1} as the error value. Even when we detected in our spectra some permitted lines of O I, Si II, N III and O III (Fig. 1), these lines are emitted by different mechanisms than recombination, such as fluorescence and Bowen mechanism, therefore those lines were not considered for the comparison between CELs and ORLS.

Expansion velocities (V_{exp}) were determined from the FWHM (Full Width at Half Maximum) for most of the lines which have a single component. As said in §2.1 the instrumental and thermal widths were discounted by assuming they add in quadrature. Turbulent velocities are contributing also to the FWHM. Such velocities have been analysed, among others, by [Sabbadin et al. \(2008\)](#); [Gesicki & Zijlstra \(2003\)](#); [Gesicki et al. \(2003\)](#). The latter authors concluded that turbulence is significant in PNe with [WC] central stars, but has small values in other PNe. In this paper we are analysing non-[WR] nebula, so turbulence might not be important and we have not considered it in the expansion velocity calculation.

For the lines with a double-peaked profile, a fit of two deblending Gaussian was applied, and the expansion velocities were determined from the difference in velocity of both Gaussian.

Final expansion velocity of each ion was determined as the average value of the expansion velocities of their observed CELs and ORLS. Expansion velocities vs. ionization potentials are presented in Fig. 3.

In most cases we found that the kinematic behaviour of CELs is typical of a plasma expanding in the vacuum. That is, the expansion velocity increases with the distance to the central star, which is normally predicted for a plasma expanding with velocities style Hubble-flow.

The analysis of Fig. 3 for the different objects is presented in the next section where a brief description of the objects is included, and we discuss the abundance results and the kinematics obtained.

Radial velocities (V_{rad}) were determined for each observed line by using Doppler effect. The heliocentric correction was applied to all the observed velocities and they were averaged to get a systemic velocity for each object. These values and their standard deviations are presented in Table 12.

Table 9. Ionic abundances from ORLs

Multiplet	λ_0	Cn 3-1	Vy 2-2	Hu 2-1	Vy 1-2	IC 4997
He^+/H^+						
	5875	0.054±0.002	0.115±0.001	0.107±0.004	0.900±0.008	0.146±0.005
$\text{He}^{+2}/\text{H}^+$						
	4686	—	—	—	0.030±0.001	—
$\text{O}^{+2}/\text{H}^+ (\times 10^{-4})$						
V1	4638	—	5.09±1.42	4.50±0.65	—	7.25±2.20
	4641	—	3.83±0.41	5.06±0.42	40.90±8.27	8.47±1.12
	4649	—	6.47±1.30	3.45±0.30	28.54 ^{3.23} _{-1.59}	8.25±1.20
	4650	—	9.24 ^{4.78} _{-5.79}	—	18.22±8.10	7.76±2.05
	4661	—	6.41±0.93	3.44 ^{0.53} _{-0.65}	26.81±8.75	7.31±1.09
	4673	—	—	—	81.13 ^{58.58} _{-47.71}	—
	4676	—	—	3.92±0.71	—	6.68±1.58
	4696	—	—	—	—	—
	<i>V1 sum</i>	—	5.50±0.71	3.93±0.19	30.95±2.90	8.54±0.61
$\text{C}^{+2}/\text{H}^+ (\times 10^{-4})$						
6	4267	1.15±0.27	3.00±0.55	3.70±0.20	8.56±2.60	1.81±0.34
$\text{N}^{+2}/\text{H}^+ (\times 10^{-4})$						
V3	5667	—	3.39±0.61	1.90±0.38	—	2.77±0.74
	5676	—	—	2.11±0.75	—	—
	5679	—	—	1.38±0.21	3.55±1.78	1.14±0.51
	5711	2.09±0.95	—	—	—	—
		<i>V3 sum</i>	1.99±0.90	4.18±0.70	1.73±0.20	3.40±1.68

8 DISCUSSION OF INDIVIDUAL RESULTS

8.1 Cn 3-1

This is a dense and compact PN, with a low ionization degree corroborated by the low [O III] $\lambda 5007/\text{H}\beta$ flux ratio of 0.28, therefore almost all the oxygen is as O^+ . The nebula shows a low expansion velocity of about 12 km s⁻¹ from the [O III] $\lambda 5007$ line (see Fig. 3), and a heliocentric velocity of +29.62±6.37 km s⁻¹ (Table 12).

Its distance from GAIA DR2 (7.65 kpc) and morphology from Sahai et al. (2011) were already presented in Table 1.

Physical conditions and chemical abundances were derived previously for this nebula by Milingo et al. (2010) and Wesson et al. (2005). Our values are very similar to those of both authors (see Table 13). The O abundance of $12 + \log(\text{O}/\text{H}) = 8.60$, together with the heliocentric velocity, indicate that this is a disc nebula, located in the solar vicinity. As a new result we have determined the Ne abundance in this object, with a value $\log(\text{Ne}/\text{O}) \sim -1.82$, which results to be very low in comparison with what is expected for normal PNe. There are only a handful of PNe with such a low Ne/O abundance ratio. The value reported for Cn 3-1 is similar to the value reported for the halo PN H 4-1 (Otsuka & Tajitsu 2013), and for the PNe M 1-14, IC 418 and Mz 3 (Henry et al. 2010; Stanghellini & Haywood 2010). No reliable explanation has been offered so far for this phenomenon.

No ADF has been derived for this nebula previously. In this work we could not derive an ADF either, because the O^{+2} abundance from ORLs could not be determined due to the low ionization degree of the nebula and due to the presence of stellar emission lines in the wavelength range where the most important O II lines (multiplet V1) are found.

Regarding the kinematic behaviour, the blue points in Fig. 3 (up, left) show that low ionization CELs from [S II], [N II], and [O II] present higher expansion velocities (from 18 to 21 km s⁻¹) than higher ionization CELs showing V_{exp} lower than 15 km s⁻¹. This behaviour is typical of an ionized plasma expanding in vacuum, accelerating with the distance to the central star. The red dots in this figure, showing the expansion velocities given by the ORLs, present a similar behaviour to that of CELs (increasing velocity with distance to the central star), except for N II which shows a too large velocity for its ionization potential. However, considering the large error bars, N II velocity coincides with ions of similar ionization potential. It should be noticed that the O II recombination lines and [O III] collisionally excited lines present a very similar expansion velocity. Therefore, from these results there is no evidence of different plasmas with different kinematics producing recombination lines and collisionally excited lines in Cn 3-1.

8.2 Vy 2-2

This is a very compact, young and dense nebula. It shows a heliocentric radial velocity of -63.91 ± 6.60 km s⁻¹ (this work). The distance from Frew et al. (2016), the morphology from Sahai et al. (2011), the central star classification and the previous reported ADFs, as well as the huge FWZI at the base of H α were presented in Table 1.

The He II $\lambda 4686$ recombination line was detected here showing a wide profile, therefore we consider it of stellar origin. Our diagnostic diagram indicates an external zone with density of $n_e([\text{S II}]) = 6,200$ cm⁻³, and an inner zone of very high density with values $n_e([\text{Cl III}])$ of about 58,200 cm⁻³, while the [N II] and the [Ar IV] temperature

Table 10. Ionic and total abundances from CELs. He/H total abundances from ORLs are also presented.

Ion	Cn 3-1	Vy 2-2	Hu 2-1	Vy 1-2	IC 4997
O ⁺ ($\times 10^{-5}$)	37.10 ^{+11.92} _{-6.67}	1.39 ^{+0.43} _{-0.29}	5.70 ^{+8.89} _{-5.70}	1.57 ^{+1.47} _{-0.95}	0.72 ^{+1.23} _{-0.38}
O ⁺² ($\times 10^{-4}$)	0.22 \pm 0.02	1.22 ^{+0.51} _{-0.13}	2.12 ^{+2.84} _{-0.76}	5.65 ^{+1.47} _{-0.95}	1.72 ^{+1.99} _{-0.79}
ICF(O)	1.00	1.00	1.00	1.17 \pm 0.02	1.00
N ⁺ ($\times 10^{-5}$)	6.24 ^{+0.80} _{-0.59}	0.55 \pm 0.05	1.86 ^{+1.38} _{-0.48}	0.66 ^{+0.17} _{-0.11}	0.17 ^{+0.12} _{-0.06}
ICF(N)	1.06 \pm 0.01	10.28 ^{+3.74} _{-2.45}	3.99 ^{+0.70} _{-0.55}	44.45 ^{+10.35} _{-13.34}	24.37 ^{+6.54} _{-5.55}
Ne ⁺² ($\times 10^{-5}$)	0.03 \pm 0.01	3.34 ^{+1.16} _{-0.34}	2.54 ^{+3.53} _{-0.95}	9.84 ^{+2.73} _{-2.09}	3.78 ^{+3.03} _{-1.47}
Ne ⁺³ ($\times 10^{-4}$)	—	—	—	3.82 ^{+3.88} _{-1.98}	—
ICF(Ne)	17.45 ^{+3.71} _{-2.20}	1.11 \pm 0.04	1.33 \pm 0.07	1.20 \pm 0.02	1.04 \pm 0.01
Ar ⁺² ($\times 10^{-6}$)	—	2.73 ^{+0.22} _{-0.15}	1.10 ^{+1.97} _{-0.45}	—	0.47 ^{+0.33} _{-0.15}
Ar ⁺³ ($\times 10^{-7}$)	—	0.16 ^{+0.06} _{-0.03}	0.19 ^{+0.25} _{-0.06}	14.79 ^{+4.22} _{-2.77}	1.91 ^{+2.30} _{-0.87}
Ar ⁺⁴ ($\times 10^{-8}$)	—	—	—	1.34 ^{+0.40} _{-0.36}	—
ICF(Ar)	—	1.11 \pm 0.04	1.33 \pm 0.08	1.02 \pm 0.01	1.04 \pm 0.01
S ⁺ ($\times 10^{-7}$)	17.06 ^{+4.70} _{-2.52}	0.51 ^{+0.14} _{-0.08}	1.58 ^{+1.02} _{-0.45}	3.97 ^{+2.30} _{-1.01}	1.81 ^{+2.34} _{-0.78}
S ⁺² ($\times 10^{-6}$)	4.12 ^{+0.62} _{-0.42}	12.76 ^{+1.58} _{-1.38}	1.74 ^{+2.51} _{-0.60}	3.85 ^{+1.51} _{-0.92}	1.17 ^{+0.81} _{-0.42}
ICF(S)	1.00 \pm 0.01	1.56 \pm 0.14	1.20 \pm 0.05	2.47 ^{+0.17} _{-0.27}	2.04 \pm 0.16
Cl ⁺² ($\times 10^{-8}$)	9.03 ^{+1.38} _{-0.97}	6.17 ^{+3.41} _{-1.27}	3.78 ^{+3.53} _{-1.04}	9.40 ^{+3.28} _{-2.29}	1.09 ^{+0.81} _{-0.38}
ICF(Cl)	1.41 \pm 0.08	1.57 \pm 0.14	1.31 \pm 0.05	2.73 \pm 0.19	2.37 \pm 0.10
Fe ⁺ ($\times 10^{-7}$)	—	3.65 ^{+0.44} _{-0.34}	—	—	—
Fe ⁺² ($\times 10^{-7}$)	3.84 \pm 0.48	7.40 \pm 0.88	1.85 ^{+2.23} _{-0.60}	—	0.48 ^{+0.27} _{-0.13}
ICF(Fe)	—	0.31 \pm 0.06	0.59 \pm 0.05	—	—
K ⁺³ ($\times 10^{-9}$)	—	—	—	16.53 ^{+7.46} _{-6.86}	1.16 ^{+0.77} _{-0.48}
ICF(K)	—	—	—	1.53 \pm 0.02	—
Total abundances in a 12+log(X/H) scale					
He/H	10.73 \pm 0.02	11.06 \pm 0.01	11.03 \pm 0.02	11.07 \pm 0.03	11.16 \pm 0.01
O/H	8.60 ^{+0.12} _{-0.08}	8.14 ^{+0.12} _{-0.05}	8.46 ^{+0.38} _{-0.20}	8.84 ^{+0.10} _{-0.08}	8.25 ^{+0.34} _{-0.26}
N/H	7.82 \pm 0.05	7.74 ^{+0.13} _{-0.09}	7.87 ^{+0.22} _{-0.12}	8.46 ^{+0.10} _{-0.11}	7.63 ^{+0.20} _{-0.15}
Ne/H	6.79 \pm 0.16	7.58 ^{+0.11} _{-0.05}	7.52 ^{+0.38} _{-0.14}	8.07 ^{+0.11} _{-0.10}	7.60 ^{+0.26} _{-0.21}
Ar/H	—	6.48 \pm 0.03	6.18 ^{+0.46} _{-0.23}	6.22 ^{+0.11} _{-0.09}	5.84 ^{+0.30} _{-0.20}
S/H	6.77 ^{+0.07} _{-0.05}	7.31 \pm 0.05	6.37 ^{+0.36} _{-0.18}	7.02 ^{+0.12} _{-0.10}	6.44 ^{+0.23} _{-0.18}
Cl/H	5.11 ^{+0.08} _{-0.06}	4.97 ^{+0.23} _{-0.11}	4.70 ^{+0.27} _{-0.13}	5.41 \pm 0.11	4.41 ^{+0.23} _{-0.18}
Fe/H	—	6.35 ^{+0.08} _{-0.06}	5.63 ^{+0.35} _{-0.16}	—	—
K/H	—	—	—	4.45 ^{+0.16} _{-0.24}	—
N/O	-0.78 ^{+0.06} _{-0.09}	-0.41 ^{+0.07} _{-0.08}	-0.60 ^{+0.11} _{-0.18}	-0.38 ^{+0.10} _{-0.15}	-0.62 ^{+0.15} _{-0.20}
Ne/O	-1.82 ^{+0.10} _{-0.11}	-0.56 \pm 0.02	-0.92 \pm 0.03	-0.76 \pm 0.03	-0.66 ^{+0.06} _{-0.08}
Ar/O	—	-1.65 ^{+0.06} _{-0.15}	-2.26 ^{+0.11} _{-0.07}	-2.62 \pm 0.03	-2.42 ^{+0.07} _{-0.09}
S/O	-1.82 ^{+0.04} _{-0.06}	-0.85 ^{+0.07} _{-0.13}	-2.08 ^{+0.04} _{-0.05}	-1.82 ^{+0.06} _{-0.07}	-1.81 \pm 0.52
Cl/O	-3.49 \pm 0.04	-3.16 ^{+0.11} _{-0.08}	-3.75 ^{+0.07} _{-0.12}	-3.44 \pm 0.09	-3.84 ^{+0.25} _{-0.36}
Fe/O	—	-1.80 ^{+0.07} _{-0.10}	-2.81 \pm 0.05	—	—
K/O	—	—	—	-4.39 ^{+0.16} _{-0.21}	—

Table 11. Abundance Discrepancy Factors (ADFs) of the sample

	Cn 3-1	Vy 2-2	Hu 2-1	Vy 1-2	IC 4997
O ⁺² /H ⁺ $\times 10^{-4}$ (ORLs)	—	5.50 \pm 0.71	3.93 \pm 0.19	30.95 \pm 2.90	8.54 \pm 0.61
O ⁺² /H ⁺ $\times 10^{-4}$ (CELs)	0.22 \pm 0.02	1.22 ^{+0.51} _{-0.13}	2.12 ^{+2.84} _{-0.76}	5.65 ^{+1.47} _{-0.95}	1.72 ^{+1.99} _{-0.79}
ADF(O ⁺²)	—	4.30 ^{+1.00} _{-1.16}	1.85 \pm 1.05	5.34 ^{+1.27} _{-1.08}	4.87 ^{+4.34} _{-2.71}

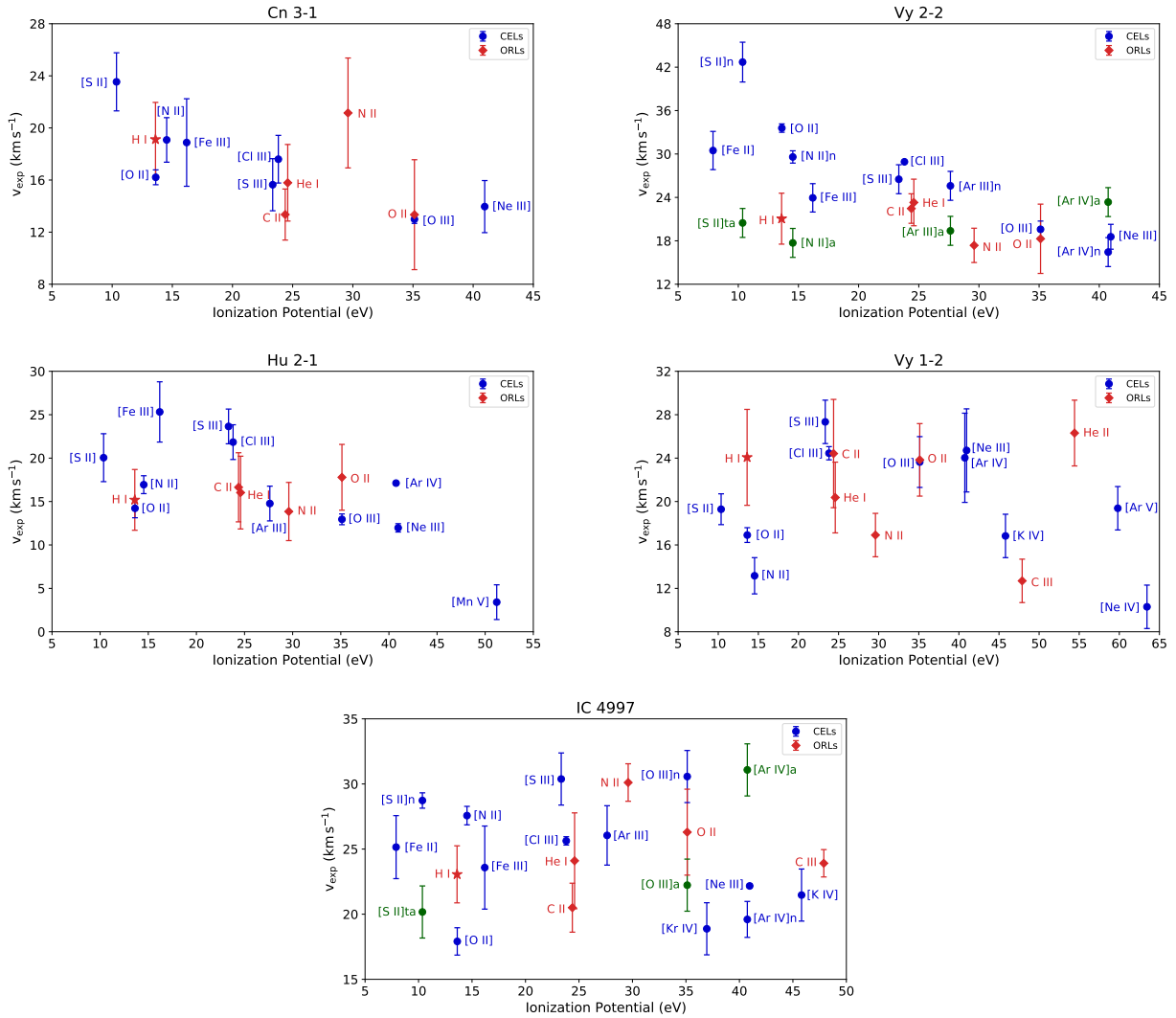


Figure 3. Expansion velocity vs. ionization potential of different ions, for the objects studied here. Expansion velocities derived from CELs are in blue, expansion velocities from ORLs are in red. In the cases of Vy 2-2 and IC 4997, the nebular and auroral lines of some ions are marked in green as they show different expansion velocities.

Table 12. Heliocentric radial velocities for the sample of PNe.

Object	V_{rad}
Cn 3-1	$+29.62 \pm 6.37$
Vy 2-2	-63.91 ± 6.60
Hu 2-1	$+23.62 \pm 5.67$
Vy 1-2	-82.40 ± 7.87
IC 4997	-58.36 ± 9.91

sensitive diagnostic lines are indicating densities of about $10^5 - 10^6 \text{ cm}^{-3}$. Therefore a steep density gradient exists in this nebula. Electron temperatures could be derived from [O III] and [Ar III] CELs providing values of $T_e(\text{[O III]}) = 12,800 \text{ K}$ and $T_e(\text{[Ar III]}) = 8,800 \text{ K}$. The high electron density prevents temperature determination from the [N II] $\lambda\lambda(6548+6584)/5755$ lines ratio.

The abundances derived for this nebula indicate a low-abundance object with $12 + \log(\text{O}/\text{H}) = 8.14$, while it presents about solar N, Ne, S, Ar, and Cl abundances. The abundances found in the literature

by Perinotto et al. (2004) and Wesson et al. (2005) are in general agreement with our values (Table 13). The low O abundance could be due to depletion in dust grains, and since the S abundance is not largely depleted, the dominant dust in Vy 2-2 might be the one of dual-chemistry (DC) (García-Hernández & Górný 2014). We also found a $12 + \log(\text{Fe}/\text{H}) = 6.35^{+0.08}_{-0.06}$, which is lower than the solar value of 7.46, this can be also an indicator of depletion into dust grains (García-Rojas et al. 2013, and references therein). The ADF(O^{+2}) derived in this work for O^{+2} is $4.30^{+1.00}_{-1.16}$, which is significantly lower than the value 11.8 reported by Wesson et al. (2005).

The expansion velocities of the different ions, derived from the FWHM of lines, are presented in Fig. 3 (up, right). It is found that CELs (blue dots) show a velocity field increasing with the distance from the central star, from about 19 km s^{-1} in the Ar^{+3} and Ne^{+2} zones to about 34 km s^{-1} or larger in the zone where O^+ , S^+ and Fe^{+2} reside, while ORLs present slightly lower V_{exp} , and no clear gradient is found. The [O III] lines show $V_{\text{exp}} = 18 \text{ km s}^{-1}$, while the O II lines show $V_{\text{exp}} = 15 \text{ km s}^{-1}$, which can be considered equal within uncertainties.

An interesting issue occurring in this nebula, and also in IC 4997, is that the auroral and trans-auroral lines, shown in green in Fig. 3 (up, right) (e.g., [N II] λ 5755, [S II] λ 4068, [Ar III] λ 5192) present lower expansion velocities than the nebular lines of the same ion ([N II] λ 6584, 6548, [S II] λ 6716, 6731, [Ar III] λ 7135). The differences in velocity are larger than the uncertainties. Exceptions are the lines of [Ar IV] which show the opposite, the auroral line λ 7170 presents slightly larger expansion velocity than the nebular line λ 4740, however both velocities are similar within uncertainties. A possible explanation for this peculiar phenomenon is associated with the very high density gradient in this nebula. It is known that auroral lines usually have critical densities larger than the nebular lines thus, in very high density nebulae the auroral lines can be emitted in denser zones nearer the central star, where nebular lines are undergoing collisional de-excitation. These inner zones are expanding more slowly, in a Hubble-type flow. A more detailed discussion on this subject can be found in §8.6.

8.3 Hu 2-1

Chemical abundances for this object have been reported by Henry et al. (2010), Perinotto et al. (2004), Wesson et al. (2005) and Delgado-Inglada et al. (2015). Their results are in agreement with the values reported here (Table 13). With a heliocentric velocity of $+23.62 \pm 5.67$ km s⁻¹ and $12 + \log(\text{O}/\text{H}) = 8.46$, Hu 2-1 is a regular disc PN in the Galaxy. Wesson et al. (2005) reported an ADF(O⁺²) of 4.00, while we have found an ADF(O⁺²) of 1.85 ± 1.05 . A discussion on this and other differences is presented in §9.

This and Vy 2-2 are the only objects in the sample in which we can determine an iron total abundance using the ICF given by Rodríguez & Rubin (2005), in the other objects their parameters are outside the ICF validity range. We found a value of $12 + \log(\text{Fe}/\text{H}) = 5.63$, which is much lower than the solar value of $12 + \log(\text{Fe}/\text{H}) = 7.46$ and, as for Vy 2-2, may be indicative of iron depletion into dust (García-Rojas et al. 2013, and references therein), although O and S do not appear very depleted.

The kinematic behaviour of CELs (blue points in Fig. 3 (middle, left)) is consistent with a Hubble-flow type expansion, as V_{exp} of [N II], [S II], [O II] and [S III] lines are larger than V_{exp} of higher ionized species. V_{exp} of ORLs (red points) seem to show a flatter gradient. The velocity of O II ORLs appears slightly higher than V_{exp} of [O III] CELs but equal within uncertainties.

8.4 Vy 1-2

This is a young PN with a complex morphology. Akras et al. (2015) carried out a deep study of this object analysing its morphology, kinematics and chemistry. According to these authors the central star can be classified as a binary weak-emission-line star, *wels*, as it presents weak emission lines of C II, C IV and O III. Its effective temperature is in the range from 7.5×10^4 to 1.19×10^5 K. A possible very late thermal pulse (VLTP) could have occurred in the central star. From their low-resolution spectrum Akras et al. (2015) report a solar abundance of O, slightly enhanced N and depleted C.

In this work we derived a heliocentric radial velocity of -82.40 ± 7.87 km s⁻¹. Considering the distance reported by Frew et al. (2016) (8.13 kpc) and by Akras et al. (2015) (9.7 kpc), and the heliocentric velocity, this PN could be a halo object as a height of 3.3 – 3.9 kpc above the galactic plane is derived from its galactic latitude $b = +24^\circ$. However it shows an abundance $12 + \log(\text{O}/\text{H}) = 8.84$ (see Table 10) which is too large for a halo PN. This PN shows $\log(\text{N}/\text{O})$

abundance ratio of -0.38 , $\log(\text{Ne}/\text{O}) = -0.76$, $\log(\text{S}/\text{O}) = -1.82$, $\log(\text{Ar}/\text{O}) = -2.62$, and $\log(\text{Cl}/\text{O}) = -3.44$. Compared to average values for disc PN abundances given by Kingsburgh & Barlow (1994), Vy 1-2 abundances seem typical of a disc PN.

For this object, we did not detect any Ar⁺² lines in our spectra. As we determined the total abundance by using Kingsburgh & Barlow (1994) ICF, which takes into account the ionic abundances of Ar⁺², Ar⁺³ and Ar⁺⁴, our total Ar/H abundance should be considered as a lower limit, but closer to the real abundance; our value is consistent with those derived by Wesson et al. (2005) and Akras et al. (2015).

We found a $12 + \log(\text{K}/\text{H})$ ratio of $4.45^{+0.16}_{-0.24}$ which is lower than the solar value by about a factor of ~ 5.1 ; however, the ICF used to correct the observed K⁺³ abundance, which is based on the ionic fraction of Ar⁺³, requires a reliable determination of Ar/H abundance (Amayo et al. 2020, and references therein). Therefore, our K/H value should be also considered as a lower limit of the real abundance.

Wesson et al. (2005) reported an ADF(O⁺²) of 6.17 for this nebula. In this work we derived a value ADF(O⁺²) of $5.34^{+1.27}_{-1.08}$ which is consistent with their value.

The kinematics of Vy 1-2 is peculiar (Fig. 3 middle-left). Because a central ring is the brightest structure (Akras et al. 2015), the lines detected are mainly emitted in this zone. Expansion velocities provided by CELs show no gradient, actually the expansion velocities of ions in the inner zone (He⁺², Ar⁺³, Ne⁺², O⁺²) are larger than the velocities in the outer zone (N⁺, O⁺, S⁺), which is opposite of what is expected in an expanding PN following a Hubble-law flow. Only the very inner ions (Ar⁺⁴, Ne⁺³) present low expansion velocities. Velocities from ORLs show no systematic behaviour either, being some times lower and sometimes higher than CELs velocities. Therefore the inner zone seems to be accelerated compare to the outer zone. In the literature few PNe present this peculiar kinematic behaviour; considering the 14 objects studied by Peña et al. (2017) and the 40 objects analysed by Medina et al. (2006) only two of them, PN BD+30 3639 and PN M 1-32, show a similar behaviour with V_{exp} of [O III] and other high ionized species larger the V_{exp} of [N II], putting in evidence high velocity gas in the central zone.

8.5 IC 4997

This is a very young and dense nebula, whose central star, classified as *wels*, has presented important changes and where the nebula is also changing, heating with time. Kostyakova & Arkhipova (2009) monitored the spectral evolution of this object for forty years. They claimed that the electron density increased from 4×10^5 to 2×10^6 cm⁻³, and the electron temperature increased from 12,000 K to 14,000 K in the period 1972 to 1992. By considering the He I, [Ne III], and [O III] lines it is found that the nebular ionization degree has been growing with time. The central star seems to have increased its effective temperature from 37,000 – 40,000 K to 47,000 K in the same period.

IC 4997 was studied by Arrieta & Torres-Peimbert (2003), who measured a FWZI(H α) equivalent to 5,100 km s⁻¹ attributed to Raman scattering. This was also suggested by Lee & Hyung (2000). Feibelman et al. (1992) reported a secondary emission component, displaced by -69 km s⁻¹ from the peak of the broad main body of H α .

Flower (1980) analysed this object from UV and optical spectra, founding abundances $12 + \log(\text{O}/\text{H}) = 8.04$ and $12 + \log(\text{C}/\text{H}) = 7.65$. In this work we derived $12 + \log(\text{O}/\text{H}) = 8.25^{+0.34}_{-0.26}$ and an ADF(O⁺²) of $4.87^{+4.34}_{-2.71}$. Then this object is O under-abundant relative to the Sun.

Flower (1980) attributed the low C and O abundances to the pos-

sibility that an important amount of these elements could be embedded in dust grains. In this work we find that S is also slightly under-abundant which might indicate that also S could be embedded in dust grains. Even when we found abundances of Fe^{+2} and K^{+3} , we could not use the previous ICF to determine total abundances because they are outside their validity range.

The kinematics of IC 4997 is very complex. No gradient of CELs or ORLs expansion velocities are found. The same as in the case of Vy 2-2, the auroral and trans-auroral lines show lower expansion than the nebular lines of the same ion. Again this phenomenon can be attributed to the extreme density gradient in this nebula, which has a density of about $30,000 \text{ cm}^{-3}$ in the periphery and larger than about 10^6 cm^{-3} in the inner zone. The auroral and trans-auroral lines would be mainly produced in a higher density zone, where nebular lines are undergoing collisional de-excitation due to they have lower critical densities. A more detailed discussion on this subject can be found in next subsection.

8.6 Nebular and auroral line kinematics in Vy 2-2 and IC 4997

As we mentioned in the previous subsections, in Vy 2-2 and IC 4997, auroral (trans-auroral) and nebular lines of [S II], [N II], [O III], [Ar III] and [Ar IV] present different profiles and therefore different kinematic behaviour.

From very high-resolution spectra of PN NGC 6153, Barlow et al. (2006) found that nebular and auroral lines of [O III] $\lambda 5007$ and $\lambda 4363$ present different velocity profiles. Since electronic temperature is estimated from this ratio, the authors argued that large variations in velocity of this ratio may be indicative of temperature fluctuations in the nebula. From photoionization models, Zhang (2008) explored if the differences between auroral and nebular lines profiles can be attributed to temperature or density variations in the plasma; he argues that if these effects are present in the nebulae, lines with different critical densities or excitation temperatures would show different profiles.

We attribute the velocity differences between auroral and nebular lines in Vy 2-2 and IC 4997 to density variations and not to temperature variations because in both nebulae we found a strong density gradient increasing into their inner zones and the differences in velocity are strongly marked in lines which are not useful to determine electronic temperatures, such as [S II] $\lambda\lambda(6716 + 6731)/4068$ and [N II] $\lambda\lambda(6548 + 6584)/5755$ which in the present circumstances are sensitive to density. To analyse better this phenomenon, we compare the critical densities and the expansion velocities of the auroral and nebular lines for these two objects (Fig. 4) in order to find a possible correlation between both parameters.

For Vy 2-2 (Fig. 4, left) we found that auroral lines, which have critical densities larger than 10^6 cm^{-3} , are concentrated in a zone with expansion velocities between 17 and 27 km s^{-1} . Nebular lines of [S II] and [N II] have larger expansion velocities than their auroral (trans-auroral) lines, by about 20 and 12 km s^{-1} respectively. For the cases of [Ar III], [O III] and [Ar IV] lines, the differences between auroral and nebular lines are not so considerable: for [Ar III] V_{exp} of the auroral line is 6 km s^{-1} higher than the nebular value, however considering the errors of V_{exp} of [Ar III] lines the difference is just 2 km s^{-1} ; in the case of [O III], auroral and nebular lines show the same expansion velocities of about 20 km s^{-1} ; while for [Ar IV], which shows the opposite behaviour, the velocity of the auroral line is 6 km s^{-1} larger than the nebular but considering the errors the difference is just of 2 km s^{-1} . As we showed in Fig. 3, Vy 2-2 presents a Hubble-type flow for expansion velocities of ions, therefore we can consider that

auroral lines arises from inner zones of the nebula due to their lower expansion velocities, these inner zones have higher density and the emission of lines with low critical densities is suppressed there. This effect can be found in the nebular-auroral line ratios of [S II], [N II] and [Ar IV], which are sensitive to density instead of temperature (see Fig. 2); nonetheless the density in inner zones of the nebula is not enough to overpass the critical densities of auroral lines of [Ar III] and [O III] ($n_{\text{crit}} > 10^{7.38}$) and so their line ratios are still sensitive to temperature.

For IC 4997 (Fig. 4, right), there is clear discrepancy between the velocities of the auroral and nebular lines of [S II], [O III] and [Ar IV], the differences are of 11 , 8 and 12 km s^{-1} , respectively; as in the case of Vy 2-2, [Ar IV] auroral line shows larger velocity than the nebular one. Auroral and nebular lines of [N II] and [Ar III] show the same expansion velocities (within the errors) of 27 and 25 km s^{-1} . As in Vy 2-2, for the ions which show important kinematic discrepancies between auroral and nebular lines, their auroral-nebular ratio is not sensitive to temperature and it is sensitive to density. Given the kinematic complexity of the nebula, which does not follow a Hubble-type flow (Fig. 3), it is not possible to determine if the differences of velocities of the lines are indicative of inner or outer zones of the nebula, and they might be corresponding to complex structures within the nebula.

9 DISCUSSIONS AND CONCLUSIONS

From high-resolution spectra, physical conditions (temperature and density) and chemical abundances from CELs and ORLs have been determined for the PNe Cn 3-1, Vy 2-2, Hu 2-1, Vy 1-2 and IC 4997, for which our main goal was to derive the ADFs(O^{+2}). The five objects are young and dense, show density gradients growing towards the inner zone and they have different ionization degree and different morphology. Abundance determinations of He, O, N, Ne, Ar, S, Cl have been obtained from CELs and our values are in general agreement with values previously reported in the literature.

Three of the objects, Cn 3-1, Hu 2-1, and Vy 1-2, possess typical abundances of disc PNe, comparable to the solar values. Vy 2-2 and IC 4997 are low-abundance objects with $12+\log(\text{O}/\text{H})$ of about 8.2 or lower, which can be attributed to O depletion in dust grains or to central stars formed in a low abundance medium. The large values of Ne/O, Ar/O and S/O presented by both nebulae better indicate that O might be depleted in dust grains. We also were able to determine abundances of K/H for Vy 1-2 and Fe/H for Vy 2-2 and Hu 2-1.

From comparison of chemical abundances from CELs and ORLs, ADFs(O^{+2}) were calculated for Vy 2-2, Hu 2-1, Vy 1-2 and IC 4997, obtaining values of 4.30 , 1.85 , 5.34 and 4.87 respectively. For Vy 2-2 and Hu 2-1, our values resulted to be smaller than values previously reported in the literature. The difference between our values and the previously reported can be attributed to the selection of multiplets to determine the abundances for O II. In our calculations we have determined this abundance using the lines of multiplet V1 only, which is the strongest among O II multiplets; the lines from other multiplets (e.g., V2, V5, V10, V19, V20 and 3p-4f transitions) are much fainter than those from V1 and higher errors are expected in O II abundance. The Vy 2-2, Hu 2-1 and Vy 1-2 O II abundances determined by Wesson et al. (2005) include the contribution of other multiplets. We found that our O II V1 abundances for these objects are similar to those derived by Wesson et al. (2005) for the same multiplet. However, when these authors include the contribution of the other multiplets, their O II abundances become higher leading to higher ADFs values. On the other side, Wesson et al. (2005) did not

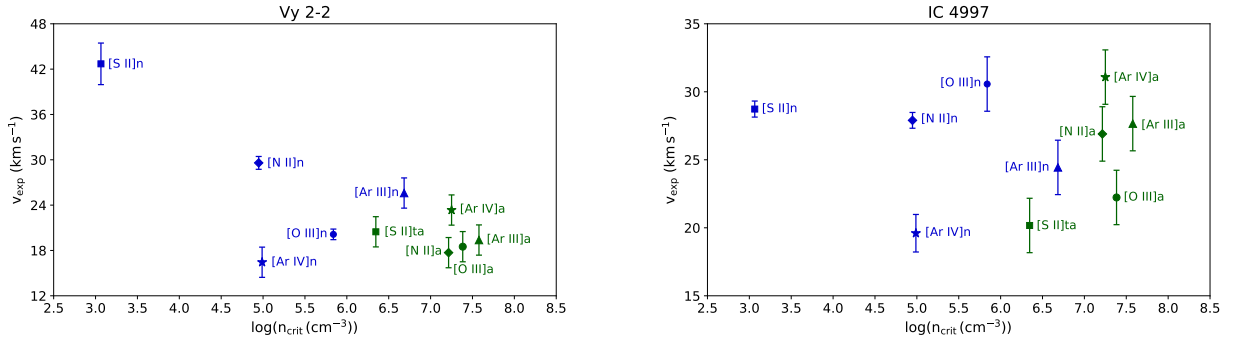


Figure 4. Expansion velocity vs. critical density (log scale) of nebular and auroral lines of [S II], [N II], [O III], [Ar III] and [Ar IV] in Vy 2-2 and IC 4997. Expansion velocities from nebular lines are in blue, expansion velocities from auroral are in green.

Table 13. Comparison of total abundances in $12+\log(X/H)$ scale^{a,b,c}

	Cn 3-1 This work	Cn 3-1 M10	Cn 3-1 W05	Vy 2-2 This work	Vy 2-2 P04	Vy 2-2 W05	Hu 2-1 This work	Hu 2-1 DI15	Hu 2-1 W05	Vy 1-2 This work	Vy 1-2 A15	Vy 1-2 W05	IC 4997 This work
He/H	10.73±0.02	10.74	10.65	11.06±0.01	10.88	11.03	11.03±0.02	10.91	10.90	11.08±0.03	11.04±0.03	11.03	11.16
O/H	8.60 ^{+0.12} _{-0.08}	8.59	8.63	8.14 ^{+0.12} _{-0.13}	8.16	7.98	8.46 ^{+0.38} _{-0.20}	8.30	8.51	8.84 ^{+0.10} _{-0.08}	8.66±0.04	8.70	8.25
N/H	7.82±0.05	7.89	7.87	7.74 ^{+0.13} _{-0.09}	7.42	7.83	7.87 ^{+0.11} _{-0.12}	7.73	7.74	8.46 ^{+0.10} _{-0.11}	8.13±0.05	8.06	7.63
Ne/H	6.79±0.16	—	—	7.58 ^{+0.11} _{-0.05}	—	7.24	7.52 ^{+0.38} _{-0.14}	7.71	7.45	8.07 ^{+0.11} _{-0.10}	—	8.00	7.60
Ar/H	—	5.83	6.09	6.48±0.03	6.05	5.88	6.18 ^{+0.46} _{-0.23}	5.81	5.78	6.22 ^{+0.11} _{-0.09}	6.28±0.06	6.25	5.84
S/H	6.77 ^{+0.07} _{-0.05}	6.96	—	7.31±0.05	6.38	6.65	6.37 ^{+0.36} _{-0.18}	—	6.10	7.02 ^{+0.12} _{-0.10}	6.80±0.08	6.78	6.44
Cl/H	5.11 ^{+0.08} _{-0.06}	5.33	—	4.97 ^{+0.23} _{-0.11}	—	—	4.70 ^{+0.27} _{-0.13}	4.68	4.59	5.38±0.18	5.22±0.12	—	4.41
N/O	-0.78 ^{+0.06} _{-0.09}	-0.70	-0.76	-0.41 ^{+0.07} _{-0.08}	-0.74	-0.15	-0.60 ^{+0.11} _{-0.18}	-0.57	-0.77	-0.38 ^{+0.10} _{-0.15}	-0.53±0.06	-0.64	-0.62
Ne/O	-1.82 ^{+0.10} _{-0.11}	—	—	-0.56 ± 0.02	—	-0.74	-0.92 ± 0.03	-0.59	-1.06	-0.76±0.03	—	-0.70	-0.66
Ar/O	—	-2.76	-2.54	-1.65 ^{+0.06} _{-0.15}	-2.11	-2.10	-2.26 ^{+0.11} _{-0.07}	-2.49	-2.73	-2.62±0.03	-2.38±0.07	-2.45	-2.42
S/O	-1.82 ^{+0.06} _{-0.04}	-1.63	—	-0.85 ^{+0.07} _{-0.13}	-1.78	-1.33	-2.08 ^{+0.04} _{-0.05}	—	-2.41	-1.82 ^{+0.06} _{-0.07}	-1.86±0.09	-1.92	-1.81
Cl/O	-3.49 ± 0.04	-3.26	—	-3.16 ^{+0.11} _{-0.08}	—	—	-3.75 ^{+0.07} _{-0.12}	-3.62	-3.92	-3.44±0.09	-3.44±0.13	—	-3.84

^a A15: Akras et al. (2015), DI15: Delgado-Inglada et al. (2015), M10: Milingo et al. (2010), P04: Perinotto et al. (2004), W05: Wesson et al. (2005).

^b Abundances from Flower (1980) for O and C are presented in the text.

^c Solar abundances by Asplund et al. (2009) are: He/H=10.93, O/H=8.69, C/H=8.43, N/H=7.83, Ne/H=7.93, Ar/H=6.40, S/H=7.12

report errors for the abundances of each multiplet and then it is not possible to know if those differences are within their respective error bars.

Considering the ADFs, the gas emitting ORLs is enriched by a large factor, relative to the gas emitting CELs. An important work to do is to estimate the amount of nebular mass contained in the gas emitting CELs and the gas emitting ORLs, to determine the real chemical abundances in the nebulae.

The temperatures derived from recombination lines of O II are lower than the values obtained from [O III] CELs. We did not find evidence of the existence of cold H-deficient He- and heavy elements-rich small inclusions embedded in the nebulae and emitting most of ORLs as proposed by Liu et al. (2000); Liu (2006, 2012), among others, because according to their results, and also results from other authors (e. g., Tsamis et al. 2004; Wesson et al. 2005), such inclusions would have temperatures of about 1,000 K or even lower. We did not find such extremely low ORLs temperatures in the PNe of our sample, for all cases we found that these temperatures are above 6,000 K.

The kinematics of the gas emitting CELs and ORLs was analysed for each nebula to study the possibility of different plasmas (with different physical conditions and spacial distribution) coexisting in the nebula and emitting the different lines. We compared in particular the expansion velocities given by CELs and ORLs emitted by O⁺.

The results indicate that such velocities are equal within uncertainties in Cn 3-1, Vy 2-2, Hu 2-1 and Vy 1-2, therefore from the kinematics point of view, there is no evidence for these lines being emitted in different zones of the nebula. But such velocities are very different in IC 4997, where we find $V_{\text{exp}}(\lambda 4959) = 29.56 \pm 2 \text{ km s}^{-1}$ and $V_{\text{exp}}(\lambda 4649) = 23.30 \pm 2 \text{ km s}^{-1}$, which might be implying that ORLs are being emitted in a different zone. According to Table 7, the density and temperature given by O⁺ recombination lines in IC 4997 are 5,000 cm⁻³ and 7,700 K which are much lower than the values derived from CELs.

As mentioned early for Vy 2-2 and IC 4997, we found the interesting fact that, in some cases, nebular and auroral (or trans-auroral) lines of the same ion (e.g., S⁺, N⁺, Ar⁺, Ar⁺, O⁺) present different expansion velocities. Auroral and trans-auroral lines (marked in green in Fig. 3) show, in general, lower V_{exp} which in the case of Vy 2-2 (showing a Hubble velocity expansion law) might be indicating that auroral lines (sensitive to density and temperature) are being emitted in a denser and inner zone than the nebular lines. This might be a consequence of, in general, nebular lines have critical densities smaller than auroral lines, therefore nebular lines are undergoing collisional de-excitation and are not emitted in dense zones. The phenomenon is very complex in IC 4997 where the auroral lines of S⁺ and O⁺ present lower V_{exp} than nebular lines, and the opposite oc-

curs in Ar⁺³. Anyway, being Vy 2-2 and IC 4997 the objects showing the highest density differences between the inner and outer zones, this phenomenon seems more related to density than to temperature effects.

IC 4997 is a very young PN, around a rapidly evolving hot post-AGB central star. This interesting object has been showing stellar and nebular evolution in short timescales, therefore it is necessary to keep tracking IC 4997 and other similar objects in order to better understand their behaviour and fast evolution towards the PN stage.

A similar work aiming to determine ADFs in PNe with different characteristics is being carried out for a number of objects. It will be published in the future.

ACKNOWLEDGEMENTS

We are indebted to Drs. Michael Richer, Christophe Morisset and Antonio Peimbert for interesting comments and suggestions along this research. We are grateful to José N. Espíritu for his help with PYNEB and to Alexia Amayo for her help with the Monte Carlo error determinations. We thank an anonymous referee for his/her careful reading of the manuscript and his/her suggestions that help to improve this work. This work is based upon observations carried out at the Observatorio Astronómico Nacional at the Sierra San Pedro Mártir (OAN-SPM), Baja California, México. We thank the daytime and night support staff at the OAN-SPM for facilitating and helping to obtain our observations. F.R.-E. acknowledges scholarship from CONACyT, México. This work received partial support from DGAPA-PAPIIT IN105020 and IN103519, UNAM.

Data Availability Statement: The data underlying this article will be shared on reasonable request to the corresponding author.

REFERENCES

Akras S., Boumis P., Meaburn J., Alikakos J., et al. 2015, *MNRAS*, **452**, 2911
 Amayo A., Delgado-Inglada G., García-Rojas J., 2020, *MNRAS*, **492**, 950
 Arkhipova V. P., Burlak M. A., Esipov V. F., Ikonnikova N. P., Komissarova G. V., 2017, *Astronomy Letters*, **43**, 831
 Arrieta A., Torres-Peimbert S., 2003, *ApJS*, **147**, 97
 Asplund M., Grevesse N., Sauval A. J., Scott P., 2009, *ARA&A*, **47**, 481
 Barlow M. J., Hales A. S., Storey P. J., Liu X. W., Tsamis Y. G., Aderin M. E., 2006, in Barlow M. J., Méndez R. H., eds, Vol. 234, *Planetary Nebulae in our Galaxy and Beyond*. pp 367–368, doi:10.1017/S1743921306003279
 Benjamin R. A., Skillman E. D., Smits D. P., 1999, *ApJ*, **514**, 307
 Butler K., Zeppen C. J., 1989, *A&A*, **208**, 337
 Cardelli J. A., Clayton G. C., Mathis J. S., 1989, *ApJ*, **345**, 245
 Delgado-Inglada G., Morisset C., Stasińska G., 2014, *MNRAS*, **440**, 536
 Delgado-Inglada G., Rodríguez M., Peimbert M., Stasińska G., Morisset C., 2015, *MNRAS*, **449**, 1797
 Espíritu J. N., Peimbert A., 2021, *MNRAS*, **508**, 2668
 Esteban C., García-Rojas J., Carigi L., Peimbert M., Bresolin F., López-Sánchez A. R., Mesa-Delgado A., 2014, *MNRAS*, **443**, 624
 Fang X., Liu X. W., 2013, *MNRAS*, **429**, 2791
 Fang X., Storey P. J., Liu X. W., 2011, *A&A*, **530**, A18
 Feibelman W. A., Aller L. H., Hyung S., 1992, *PASP*, **104**, 339
 Fowler D. R., 1980, *MNRAS*, **193**, 511
 Frew D. J., Parker Q. A., Bojčić I. S., 2016, *MNRAS*, **455**, 1459
 Froese Fischer C., Tachiev G., 2004, *Atomic Data and Nuclear Data Tables*, **87**, 1
 Galavis M. E., Mendoza C., Zeppen C. J., 1995, *A&AS*, **111**, 347
 Galavis M. E., Mendoza C., Zeppen C. J., 1997, *A&AS*, **123**, 159
 García-Hernández D. A., Górný S. K., 2014, *A&A*, **567**, A12
 García-Rojas J., Peña M., Morisset C., Mesa-Delgado A., Ruiz M. T., 2012, *A&A*, **538**, A54

García-Rojas J., Peña M., Morisset C., Delgado-Inglada G., Mesa-Delgado A., Ruiz M. T., 2013, *A&A*, **558**, A122
 García-Rojas J., Corradi R. L. M., Monteiro H., Jones D., Rodríguez-Gil P., Cabrera-Lavers A., 2016, *ApJ*, **824**, L27
 Gesicki K., Zijlstra A. A., 2003, *MNRAS*, **338**, 347
 Gesicki K., Acker A., Zijlstra A. A., 2003, *A&A*, **400**, 957
 Giles K., 1981, *MNRAS*, **195**, 63P
 Gómez-Llanos V., Morisset C., García-Rojas J., Jones D., Wesson R., Corradi R. L. M., Boffin H. M. J., 2020, *MNRAS*, **498**, L82
 Grandi S. A., 1976, *ApJ*, **206**, 658
 Hamuy M., Walker A. R., Suntzeff N. B., Gigoux P., et al. 1992, *PASP*, **104**, 533
 Henry R. B. C., Kwitter K. B., Jaskot A. E., Balick B., Morrison M. A., Milingo J. B., 2010, *ApJ*, **724**, 748
 Hyung S., Aller L. H., Feibelman W. A., 1994, *ApJS*, **93**, 465
 Kaufman V., Sugar J., 1986, *Journal of Physical and Chemical Reference Data*, **15**, 321
 Kingsburgh R. L., Barlow M. J., 1994, *MNRAS*, **271**, 257
 Kisielius R., Storey P. J., Ferland G. J., Keenan F. P., 2009, *MNRAS*, **397**, 903
 Kostyakova E. B., Arkhipova V. P., 2009, *Astronomy Reports*, **53**, 1155
 LaJohn L., Luke T. M., 1993, *Phys. Scr.*, **47**, 542
 Lamers H. J. G. L. M., Zickgraf F.-J., de Winter D., Houziaux L., et al. 1998, *A&A*, **340**, 117
 Lee H.-W., Hyung S., 2000, *ApJ*, **530**, L49
 Liu X.-W., 2006, in Barlow M. J., Méndez R. H., eds, Vol. 234, *Planetary Nebulae in our Galaxy and Beyond*. pp 219–226, doi:10.1017/S1743921306003000
 Liu X.-W., 2012, in Manchado A., Stanghellini L., Schönberner D., eds, *IAU Symposium Vol. 283, Planetary Nebulae: An Eye to the Future*. pp 131–138, doi:10.1017/S1743921312010836
 Liu X.-W., Storey P. J., Barlow M. J., Danziger I. J., et al. 2000, *MNRAS*, **312**, 585
 Liu X.-W., Luo S. G., Barlow M. J., Danziger I. J., Storey P. J., 2001, *MNRAS*, **327**, 141
 Luridiana V., Morisset C., Shaw R. A., 2015, *A&A*, **573**, A42
 McLaughlin B. M., Bell K. L., 2000, *Journal of Physics B Atomic Molecular Physics*, **33**, 597
 McNabb I. A., Fang X., Liu X.-W., Bastin R. J., et al. 2013, *MNRAS*, **428**, 3443
 Medina S., Peña M., Morisset C., Stasińska G., 2006, *Rev. Mex. Astron. Astrofis.*, **42**, 53
 Mendoza C., 1983, in Aller L. H., ed., *IAU Symposium Vol. 103, Planetary Nebulae*. pp 143–172
 Mendoza C., Zeppen C. J., 1982, *MNRAS*, **198**, 127
 Menzel D. H., Aller L. H., Hebb M. H., 1941, *ApJ*, **93**, 230
 Milingo J. B., Kwitter K. B., Henry R. B. C., Souza S. P., 2010, *ApJ*, **711**, 619
 Otsuka M., Tajitsu A., 2013, *ApJ*, **778**, 146
 Otsuka M., Tajitsu A., Hyung S., Izumiura H., 2010, *ApJ*, **723**, 658
 Peña M., Ruiz-Escobedo F., Rechy-García J. S., García-Rojas J., 2017, *MNRAS*, **472**, 1182
 Peimbert A., Peimbert M., Delgado-Inglada G., García-Rojas J., Peña M., 2014, *Rev. Mex. Astron. Astrofis.*, **50**, 329
 Pequignot D., Petitjean P., Boisson C., 1991, *A&A*, **251**, 680
 Perinotto M., Morbidelli L., Scatarzi A., 2004, *MNRAS*, **349**, 793
 Podobedova L. I., Kelleher D. E., Wiese W. L., 2009, *Journal of Physical and Chemical Reference Data*, **38**, 171
 Porter R. L., Ferland G. J., Storey P. J., Detisch M. J., 2012, *MNRAS*, **425**, L28
 Porter R. L., Ferland G. J., Storey P. J., Detisch M. J., 2013, *MNRAS*, **433**, L89
 Richer M. G., Georgiev L., Arrieta A., Torres-Peimbert S., 2013, *ApJ*, **773**, 133
 Rodríguez M., Rubin R. H., 2005, *ApJ*, **626**, 900
 Sabbadin F., Turatto M., Benetti S., Ragazzoni R., Cappellaro E., 2008, *A&A*, **488**, 225
 Sahai R., Morris M. R., Villar G. G., 2011, *AJ*, **141**, 134

Table A1. Atomic parameters used in PYNEB calculations

Ion	Transition probabilities	Collisional strenghts
N ⁺	Froese Fischer & Tachiev (2004)	Tayal (2011)
O ⁺	Froese Fischer & Tachiev (2004)	Kisielius et al. (2009)
O ⁺²	Froese Fischer & Tachiev (2004) Storey & Zeippen (2000)	Storey et al. (2014)
Ne ⁺²	Galavis et al. (1997)	McLaughlin & Bell (2000)
Ne ⁺³	Zeippen (1982)	Giles (1981)
S ⁺	Podobedova et al. (2009)	Tayal & Zatsarinny (2010)
S ⁺²	Podobedova et al. (2009)	Tayal & Gupta (1999)
Cl ⁺²	Mendoza (1983)	Butler & Zeippen (1989)
Ar ⁺²	Mendoza (1983) Kaufman & Sugar (1986)	Galavis et al. (1995)
Ar ⁺³	Kaufman & Sugar (1986)	Mendoza & Zeippen (1982)
Ar ⁺⁴	LaJohn & Luke (1993) Mendoza & Zeippen (1982) Kaufman & Sugar (1986)	Galavis et al. (1995)
K ⁺³	Mendoza (1983) Kaufman & Sugar (1986)	Galavis et al. (1995)

Ion	Effective recombination coefficients
H ⁺	Storey & Hummer (1995)
He ⁺	Porter et al. (2012, 2013)
He ⁺²	Storey & Hummer (1995)
N ⁺²	Fang et al. (2011)
O ⁺²	Storey et al. (2017)
C ⁺²	Pequignot et al. (1991)

Schuster W. J., Parrao L., 2001, *Rev. Mex. Astron. Astrofis.*, **37**, 187
 Stanghellini L., Haywood M., 2010, *ApJ*, **714**, 1096
 Storey P. J., Hummer D. G., 1995, *MNRAS*, **272**, 41
 Storey P. J., Zeippen C. J., 2000, *MNRAS*, **312**, 813
 Storey P. J., Sochi T., Badnell N. R., 2014, *MNRAS*, **441**, 3028
 Storey P. J., Sochi T., Bastin R., 2017, *MNRAS*, **470**, 379
 Tayal S. S., 2011, *ApJS*, **195**, 12
 Tayal S. S., Gupta G. P., 1999, *ApJ*, **526**, 544
 Tayal S. S., Zatsarinny O., 2010, *ApJS*, **188**, 32
 Tresse L., Maddox S., Loveday J., Singleton C., 1999, *MNRAS*, **310**, 262
 Tsamis Y. G., Barlow M. J., Liu X. W., Storey P. J., Danziger I. J., 2004, *MNRAS*, **353**, 953
 Weidmann W. A., et al., 2020, *A&A*, **640**, A10
 Wesson R., Liu X. W., Barlow M. J., 2003, *MNRAS*, **340**, 253
 Wesson R., Liu X.-W., Barlow M. J., 2005, *MNRAS*, **362**, 424
 Zeippen C. J., 1982, *MNRAS*, **198**, 111
 Zhang Y., 2008, *A&A*, **486**, 221
 Zhang Y., Liu X. W., Liu Y., Rubin R. H., 2005, *MNRAS*, **358**, 457

APPENDIX A: ATOMIC DATA

APPENDIX B: IONIZATION CORRECTION FACTORS

ICFs used for the total abundances calculation are listed next.

- $\frac{\text{He}}{\text{H}} = \frac{\text{He}^+}{\text{H}^+}$. If He⁺² is detected $\frac{\text{He}}{\text{H}} = \frac{\text{He}^+ + \text{He}^{+2}}{\text{H}^+}$.
- $\frac{\text{O}}{\text{H}} = \text{ICF}(\text{O}) \times \frac{\text{O}^+ + \text{O}^{+2}}{\text{H}^+}$. ICF(O) = 1 if no He⁺² is detected.

Otherwise, ICF(O) is given by the equation (12) in Delgado-Inglada et al. (2014).

- $\frac{\text{N}}{\text{H}} = \text{ICF}(\text{N}) \times \frac{\text{N}^+}{\text{H}^+}$. ICF(N) = $\frac{\text{O}}{\text{O}^+}$ (Kingsburgh & Barlow 1994).
- $\frac{\text{Ar}}{\text{H}} = \text{ICF}(\text{Ar}) \times \frac{\text{Ar}^{+2} + \text{Ar}^{+3} + \text{Ar}^{+4}}{\text{H}^+}$. ICF(Ar) = $\frac{1}{1 - \text{N}^+/\text{N}}$ (Kingsburgh & Barlow 1994).

- $\frac{\text{Ne}}{\text{H}} = \text{ICF}(\text{Ne}) \times \frac{\text{Ne}^{+2}}{\text{H}^+}$. ICF(Ne) = $\frac{\text{O}}{\text{O}^{+2}}$ (Kingsburgh & Barlow 1994).

- $\frac{\text{S}}{\text{H}} = \text{ICF}(\text{S}) \times \frac{\text{S}^+ + \text{S}^{+2}}{\text{H}^+}$. ICF(S) = $\left[1 - \left(1 - \frac{\text{O}^+}{\text{O}} \right)^3 \right]^{-1/3}$. (Kingsburgh & Barlow 1994).

- $\frac{\text{Cl}}{\text{H}} = \text{ICF}(\text{Cl}) \times \frac{\text{Cl}^{+2}}{\text{H}^+}$. ICF(Cl) = $\frac{\text{S}}{\text{S}^{+2}}$ (Liu et al. 2000; Wesson et al. 2005).

- $\frac{\text{K}}{\text{Ar}} = \frac{\text{K}^{+3}}{\text{Ar}^{+3}} \times \text{ICF}(\text{K})$, ICF(K) is given by equation (11) in Amayo et al. (2020).

- $\frac{\text{Fe}}{\text{O}} = \frac{\text{Fe}^{+2}}{\text{O}^+} \times \text{ICF}(\text{Fe})$, ICF(Fe) = $1.1 \left(\frac{\text{O}^+}{\text{O}^{+2}} \right)^{0.58}$, (Rodríguez & Rubin 2005).

This paper has been typeset from a $\text{\TeX}/\text{\LaTeX}$ file prepared by the author.